

Pulmonary Lesion Classification from Endobronchial Ultrasonogram
using Adaptive Ray Tracing

Miss Wannapon Suraworachet



จุฬาลงกรณ์มหาวิทยาลัย

CHULALONGKORN UNIVERSITY

บทคัดย่อและแฟ้มข้อมูลฉบับเต็มของวิทยานิพนธ์ตั้งแต่ปีการศึกษา 2554 ที่ให้บริการในคลังปัญญาจุฬาฯ (CUIR)
เป็นแฟ้มข้อมูลของนิสิตเจ้าของวิทยานิพนธ์ ที่ส่งผ่านทางบัณฑิตวิทยาลัย

The abstract and full text of theses from the academic year 2011 in Chulalongkorn University Intellectual Repository (CUIR)
are the thesis authors' files submitted through the University Graduate School.

A Thesis Submitted in Partial Fulfillment of the Requirements
for the Degree of Master of Science Program in Computer Science and Information
Technology

Department of Mathematics and Computer Science

Faculty of Science

Chulalongkorn University

Academic Year 2014

Copyright of Chulalongkorn University

การจำแนกรอยโรคปอดจากภาพเอ็นโดบรอนเคียลที่บันทึกด้วยคลื่นเสียงความถี่สูง
โดยใช้การตามรอยรังสีที่ปรับค่าได้



วิทยานิพนธ์นี้เป็นส่วนหนึ่งของการศึกษาตามหลักสูตรปริญญาวิทยาศาสตรมหาบัณฑิต
สาขาวิชาวิทยาการคอมพิวเตอร์และเทคโนโลยีสารสนเทศ ภาควิชาคณิตศาสตร์และวิทยาการ
คอมพิวเตอร์

คณะวิทยาศาสตร์ จุฬาลงกรณ์มหาวิทยาลัย

ปีการศึกษา 2557

ลิขสิทธิ์ของจุฬาลงกรณ์มหาวิทยาลัย

Thesis Title	Pulmonary Lesion Classification from Endobronchial Ultrasonogram using Adaptive Ray Tracing
By	Miss Wannapon Suraworachet
Field of Study	Computer Science and Information Technology
Thesis Advisor	Assistant Professor Rajalida Lipikorn, Ph.D.

Accepted by the Faculty of Science, Chulalongkorn University in Partial Fulfillment of the Requirements for the Master's Degree

.....Dean of the Faculty of Science
(Professor Supot Hannongbua, Dr.rer.nat.)

THESIS COMMITTEE

.....Chairman
(Assistant Professor Nagul Cooharajanane, Ph.D.)

.....Thesis Advisor
(Assistant Professor Rajalida Lipikorn, Ph.D.)

.....External Examiner
(Suriya Natsupakpong, Ph.D.)

5572604823 : MAJOR COMPUTER SCIENCE AND INFORMATION TECHNOLOGY

KEYWORDS: ENDOBRONCHIAL ULTRASOUND / PULMONARY LESION / RAY TRACING / CLASSIFICATION / BOUNDARY DETECTION / SPLINE / DBSCAN / KMEAN / SECOND DERIVATIVE / HOMOGENEITY / CROSSVALIDATION

WANNAPON SURAWORACHET: Pulmonary Lesion Classification from Endobronchial Ultrasonogram using Adaptive Ray Tracing. ADVISOR: ASST. PROF. RAJALIDA LIPIKORN, Ph.D., 74 pp.

According to statistical data, lung cancer yields the highest mortality rate. Prior diagnosis of tumor is suggested to lower the rate, since the sooner the lesion is discovered, the more likely it has not developed to be a cancer yet. Benign and malignant lesion identification is still a doubtful field of study to be worked on. Once endobronchial ultrasound (EBUS)—a visualizing tool for an internal bronchus when performing bronchoscopy, became popular due to its advantages, an image obtained from EBUS is also interesting since it is able to reveal the histopathology characteristics of lesion by observing the image. As a result, the classification system based on EBUS image is developed and EBUS data of 96 patients are experimented in this research. The proposed system includes preprocessing on individual EBUS images, detection of lesion boundary, representative frame selection, echoic and statistical feature extraction, and classification. From the experiments, the overall results are quite promising with 68.11% average cross-validation test accuracy and 90% test accuracy of the best model.

Department: Mathematics and Student's Signature

Computer Science Advisor's Signature

Field of Study: Computer Science and
Information Technology

Academic Year: 2014

ACKNOWLEDGEMENTS

I would like to express my highest gratitude to Asst. Prof. Rajalida Lipikorn, Ph.D., my research advisor, for her seamless effort, highly competent advices ranging from technical, linguistic to mental issues, and generous supervision from the start of the project until now.

Beside my advisor, I am particularly grateful for the valuable assistance and helpful suggestions provided by Asst. Prof. Nagul Cooharajanane, Ph.D. and Suriya Natsupakpong, Ph.D., my thesis committees.

I would like to express my great appreciation to Col. Anan Wattanathum, MD. from Pulmonary and Critical Care Division, Department of Medicine, Phramongkutklao Hospital who supported me for clinical advices and research data.

My special thanks are extended to Prof. Charles T.M. Choi from National Chiao Tung university, Taiwan, my internship advisor, for his shared knowledge and experiences in problem-solving, Asst. Prof. Jaruloj Chongstitvatana, Sasipa Panthuwadeethorn and Charoenchai Sirisomboonrat for their kind supports toward machine learning.

Additionally, this project is financially supported by Centre of Excellence in Mathematics (CEM), Thailand.

Finally, I wish to thank my family and friends for their encouragement throughout my study.

CONTENTS

	Page
THAI ABSTRACT	iv
ENGLISH ABSTRACT	v
ACKNOWLEDGEMENTS	vi
CONTENTS	vii
LIST OF TABLES	x
LIST OF FIGURES	xi
CHAPTER I INTRODUCTION	1
1.1 Objectives	3
1.2 Scopes of the Work	3
1.3 Problem Formulation	3
1.4 Expected Outcomes	4
CHAPTER II LITERATURE REVIEW AND FUNDAMENTAL KNOWLEDGE	5
2.1 Literature Review	5
2.2 Fundamental Knowledge	8
2.2.1 Convert Grayscale into Binary	8
2.2.2 Major Axis Length	9
2.2.3 K-Mean Clustering	9
2.2.4 Polar Coordinate System	10
2.2.5 Density-Based Spatial Clustering of Applications with Noise (DBSCAN)	11
2.2.6 Second Order Derivatives	12
2.2.7 Cubic Spline Interpolation	12
2.2.8 Entropy	13

	Page
2.2.9 Gray-Level Co-Occurrence Matrix (GLCM).....	14
2.2.10 Ray Tracing.....	16
2.2.11 Zero Crossing.....	16
2.2.12 Artificial Neural Networks (ANNs).....	16
2.2.13 Cross Validation	17
2.2.14 Confusion Matrix.....	18
CHAPTER III METHODOLOGY.....	21
1. Preprocessing.....	21
2. Boundary Detection	23
2.1 360-Degree Iterative Maximum Intensity Detection	24
2.2 Density-Based Spatial Clustering of Applications with Noise (DBSCAN) Iteration	26
2.3 Elimination by Second Order Derivative and Global Average Intensity.....	27
2.4 Polar Coordinate System Origin Adjustment.....	28
2.5 Cubic Spline Interpolation.....	28
3. Best Frame Selection.....	28
4. Feature Extraction	29
4.1 Adaptive Ray Tracing.....	31
4.2 Crossing Count.....	32
5. Classification	36
CHAPTER IV EXPERIMENTAL RESULTS.....	38
CHAPTER V DISCUSSIONS AND CONCLUSION.....	42
REFERENCES	48

	Page
APPENDIX A Input Data	52
APPENDIX B Conference Paper.....	65
VITA.....	74



LIST OF TABLES

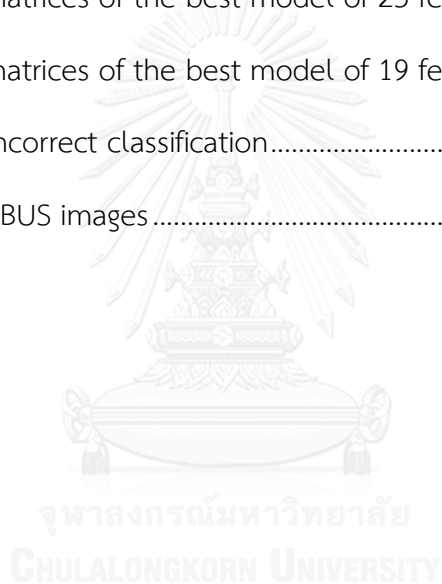
Table 1 Feature list for classification	36
Table 2 Test accuracy of every fold of 23 features	38
Table 3 Weight rank of 23 features	41
Table 4 Test accuracy of every fold of 19 features	42
Table 5 Weight rank of 19 features	44



LIST OF FIGURES

Figure 1 Bronchoscopy	1
Figure 2 Realtime image of internal bronchus obtained during bronchoscopy	2
Figure 3 Sample of an EBUS image	2
Figure 4 Samples of EBUS characteristics	6
Figure 5 Major axis	9
Figure 6 K-mean clustering	10
Figure 7 Polar coordinate system	11
Figure 8 DBSCAN	12
Figure 9 Comparison between cubic spline and interpolating cubic	13
Figure 10 Gray-level co-occurrence matrix (GLCM)	14
Figure 11 Configuration of feed-forward artificial neural networks	17
Figure 12 Cross validation	18
Figure 13 Confusion matrix	20
Figure 14 Proposed methodology	21
Figure 15 Preprocessing image	22
Figure 16 Images to be eliminated	22
Figure 17 Grayscale to binary image	23
Figure 18 360-Degree iterative maximum intensity detection	25
Figure 19 Result after DBSCAN iteration	26
Figure 20 Result of elimination by second order derivatives and average intensity	27
Figure 21 Result after spline interpolation	28
Figure 22 Result after intensity normalization	30

Figure 23 Logical mask	30
Figure 24 Best frame overlaid with a mask	31
Figure 25 After crop the image in Figure 24	31
Figure 26 4-Direction of ray tracing through an image	32
Figure 27 4-Direction ray tracing and its crossing line	34
Figure 28 Network model	37
Figure 29 Proportion of each lesion type	38
Figure 30 Confusion matrices of the best model of 23 features	40
Figure 31 Confusion matrices of the best model of 19 features	43
Figure 32 Sample of incorrect classification	45
Figure 33 Sample of EBUS images	47



CHAPTER I

INTRODUCTION

Lung cancer is known as the major cause of death cancer worldwide due to its high mortality rate [1]. Once a tumor is found in the patient's lung via radiography or other medical imaging, it tends to develop further to become a cancer which is quite too late to handle. However, if a patient can obtain a preliminary lung screening, this process can reduce the rate of mortality by 80% [2] because most of small tumors are identified as an infection or scar tissues, but not as cancer [3].

In order to diagnose lung cancer, a bronchoscopy with transbronchial lung biopsy (TBLB) is recommended due to its efficiency. The bronchoscopy is the process in which the doctor inserts a bronchoscope (a tube-liked instrument) into the patient's nose or mouth in order to explore his/her internal airways as shown in Figure 1. After that, a real-time video for capturing the interior of bronchus obtained via bronchoscopy is recorded. Figure 2 represents a sample image capturing during bronchoscopy. After the bronchoscope reaches the lesion, a forceps is introduced via bronchoscope to collect a sample tissue of the lesion. This process is known as biopsy. Then, the sample will be forwarded to examine under histopathology to diagnose and summarize the underlying properties of lesion whether it is a cancer cell.

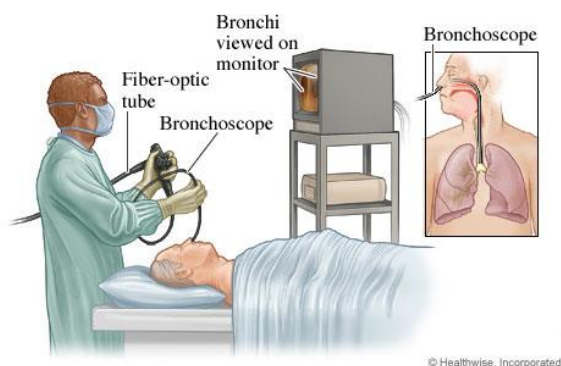


Figure 1 Bronchoscopy

(<http://www.webmd.com/lung/bronchoscopy>)



Figure 2 Realtime image of internal bronchus obtained during bronchoscopy
(http://openi.nlm.nih.gov/detailedresult.php?img=3427811_kjae-63-165-g003&req=4)

Before landing at the lesion, not only computed tomography (CT) scan is required to pre-identify lesion location within the lung, but also fluoroscopy is involved to actively locate advanced bronchoscope during operation. However, the recent study has found that a bronchoscopy that is guided by endobronchial ultrasound (EBUS) could possibly assist the doctor and generate the diagnosis yield of 60-80% [4-6], which is higher than assisting by conventional CT [4] or fluoroscopy, which can expose patients to harmful radiation [5, 7]. In general, EBUS is a device inserted via bronchoscope to visualize internal texture in real time by propagating ultrasonic waves through bronchioles and receiving reflected echoes to form a texture video. Figure 3 shows an example of an EBUS image.

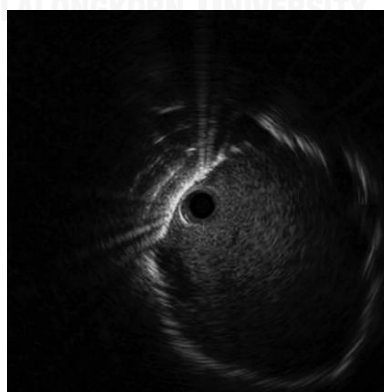


Figure 3 Sample of an EBUS image

Apart from the benefits of EBUS visualization, the characteristics of an EBUS image also have correlation with the histopathology of the lesions [8, 9]. Therefore, this discovery can possibly be a breakthrough to innovate a computer-aided

diagnosis system and thus, lower the amount of biopsy, provide less human-dependency system and lower the examination time for diagnosing further pulmonary lesions.

1.1 Objectives

To automatically classify pulmonary lesion whether it is benign or malignant based on homogeneity and other extracted features of EBUS image.

1.2 Scopes of the Work

In this study, the classification system is constrained as follows:

1. Compatible with an endobronchial ultrasonogram video input of MPEG-1 file format such as .mpg captured at 25 fps with a dimension of 576 x 720 pixels or 288 x 352 pixels.
2. Assume that the captured video of EBUS started to record when the bronchoscope reaches the lesion.
3. The size of the lesion must be larger than blood vessels.

1.3 Problem Formulation

Although there are lots of studies about EBUS characteristics and histopathology relationships, none of them has provided an automatic diagnostic tool, which relies on EBUS characteristics. The expert bronchoscopists only observe and categorize EBUS characteristics according to their experiences and then figure out the underlying relationship of histopathology and EBUS features. Thus, the purpose of this study is to construct a human-free diagnostic tool of lung cancer based on extracted features of an EBUS image.

However, there is a plenty of features to be extracted, including echoic features that have relationship with histopathology result and statistical features that are used to distinguish cancer cells in several studies [10, 11]. Our research question is to figure out which features of an EBUS image of pulmonary lesion are applicable to adapt to an automatic lung cancer diagnostic system.

1.4 Expected Outcomes

1. The proposed classification method can distinguish between benign and malignant lesions with acceptable accuracy.
2. The proposed method can help reduce the bronchoscopist-dependency on judging the characteristics of pulmonary lesion by automatically analyzing the endobronchial ultrasonogram.
3. The proposed method can assist the pathologists on verifying the results.



CHAPTER II

LITERATURE REVIEW AND FUNDAMENTAL KNOWLEDGE

In this chapter, literature review about the background of the study is provided in section 2.1, in order to demonstrate problem development and hypothesis construction of this study whereas in section 2.2, relevant techniques are discussed straightforwardly.

2.1 Literature Review

Numerous researches discovered the relationship between radiographic features and histopathology results of pulmonary nodule. Nodule size, location, growth rate, irregular margin, thickness of cavity wall, and presence of air bronchogram, are sample features extracted from radiographs to undergo pulmonary lesion classification [12-14].

However, none of them has yet developed a classification system based on echoic features—features gathered from endobronchial ultrasound (EBUS) image. Since EBUS has been found to be novel in lung cancer diagnosis, it has been very useful in medical due to its characteristics of human-friendly sound wave unlike others' harmful radiation exposure. In general, ultrasonography is a process which ultrasonic waves transmit from a transducer or a probe, travel into an area of interest, and echo back to the transducer to form a real-time image of the area as a video. Hence, echogenicity or echoic characters of the mass that varies by its density and properties leads to difference in image intensity. Ultrasound in lung or endobronchial ultrasound (EBUS) was introduced to help visualize internal bronchus and its echoic characters were found to have significant relationship with diagnosis results from histopathology. Major EBUS features to be considered in lung cancer diagnosis are homogeneity, margin continuity, and absence or presence of air bronchogram. Figure 4 (a-c) show samples of continuous margin, heterogeneity and presence of air bronchogram, respectively [15].

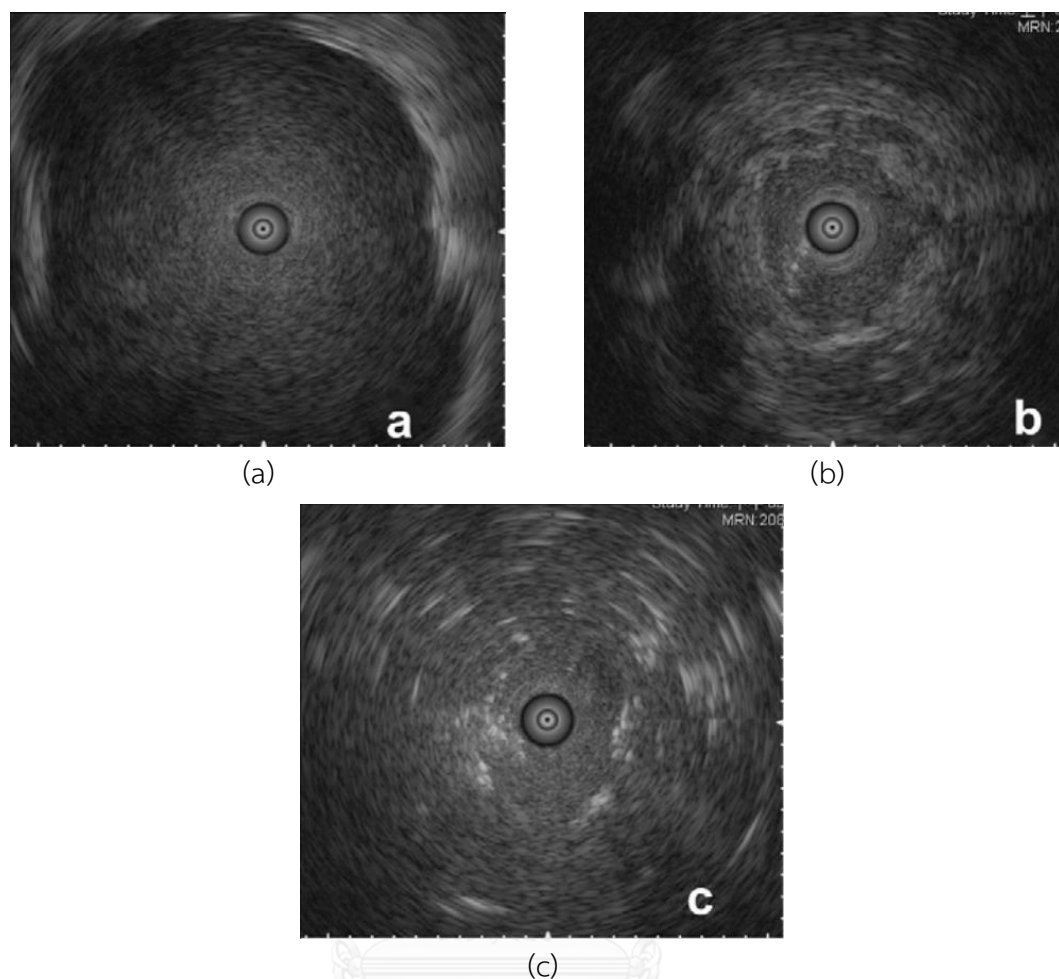


Figure 4 Samples of EBUS characteristics

(a) continuous Margin (b) heterogeneity (c) presence of air bronchogram

According to Kuo et al. [8], continuous margin, heterogeneity and absence of air bronchogram are three factors indicated malignancy of the lesions. The positive predictive value of any two out of the three factors and the negative predictive value of none of any three factors used to indicate lesion malignancy are 89.2% and 93.7%, respectively.

Although, two studies agreed that the heterogeneous pattern indicates the malignancy [8, 9], continuous margin and absence of air bronchogram arise a conflict. Kurimoto et al. suggested that non-continuous margin and air presence refer to malignant lesion [9] since cancer cells grow apart from their original cells, thus the non-continuous margin must indicate malignancy, whereas well-differentiated adenocarcinoma (WD)–one type of a cancer cell, seems to present internal air due to

its growth characteristics. This idea differs from the study of Kuo et al. which stated that the contrary features represent malignancy [8]. He argued that the cancer cell usually grows as solid. Therefore, it will conceal prior air bronchogram and reveal a sharp margin as a continuous margin on screen. Moreover, presence of air is mostly found, especially in pneumonia—a non-cancer cell, unlike a specific cancer cell as WD.

Thus, the debate is centered on the issue of which echoic features can correctly differentiate lesion malignancy and how to computerize those features to reduce human-dependency and increase consistency. Since there is still an unclarified question among which characteristic of echoic features could be integrated in pulmonary lesion classification, solely homogeneity was consensually proven as a lung cancer predictor. As a result, our classification system will attentively automate and calculate only homogeneity.

Apart from the aforementioned clinical findings, there is still work to be done on automatically generating other possible statistical features to represent lesion characteristics since multiple statistical features are found to be useful in cancer classification. According to McNitt-Gray et al. [10], gray-level co-occurrence matrix with eight levels and nine features were effectively used for feature extraction in computed tomography images of solitary pulmonary nodules. Moreover, Garra et al. [11] also supported that the use of features extracted from gray-level co-occurrence matrix, especially a combination of contrast and correlation, could possibly provide a high sensitivity in benign and malignant discriminability of ultrasonographic images in breast lesions. Hence, classification accuracy derived from an integration of clinical and statistical features could be at maximum.

Another issue arises prior to EBUS feature extraction; it is how to figure out which frame of EBUS video should be select as a patient's representative. According to Kurimoto et al. [9], an average time for EBUS is 8.38 minutes, which results in 12,570 possible images due to video frame rate of 25-frame per second. However, in traditional process of performing EBUS characteristic identification, the doctor judges its characteristics based on a single frame, which obtained manually by briefly inspecting the whole video. Therefore, to automatically manipulate best frame

selection is a part of our goal. Since the best representative frame is considered to have the largest lesion region among others, boundary detection is thus essential in order to calculate the lesion area to select a representative frame. Additionally, defining boundary is similar to defining region of interest in which will be further used for homogeneity measurement.

Various algorithms for detecting boundary have been proposed for ultrasound images used in different organs and tissues of human body, especially, in breast and prostate [16-18]. However, there is no recent study on detecting lesion boundary from EBUS. Since an EBUS image is captured within a lesion using a mechanical radial ultrasound miniature probe, the perspective of lesion is not similar to other types of ultrasound images which are mostly coronal views deriving from curvilinear ultrasound probes.

After the best representative frame is selected, and relevant features of both clinical features such as homogeneity and other statistic features are extracted, this set of features will be fed into a classifier to discover its classification accuracy and to be justified together with classifier's parameters to obtain the maximum accuracy.

2.2 Fundamental Knowledge

2.2.1 Convert Grayscale into Binary

Sometimes, only a black and white or a binary image is adequate for a specific calculation, unlike a grayscale or an RGB image, which tends to provide unnecessary information, difficult to manipulate, and time consuming. A binary image can be separated into a group of white pixels which is a group of interest, and a group of black pixels, which is a group of off-interest or refer to as background. If an image comes in a form of binary, multiple properties could be easily calculated; for instance, area, bounding box, centroid, minor axis length, major axis length, etc.

Converting a grayscale image into a binary image is done by specifying a threshold. A standard threshold is a midpoint of an intensity range. Suppose that it is an 8-bit image consists of intensities ranging between 0-255, the following pseudocode demonstrates the function of grayscale-to-binary conversion.

$$\begin{array}{ll} \text{IF } f(x, y) \geq 128, & \text{THEN } g(x, y) = 1, \\ \text{ELSE } g(x, y) = 0 & \text{END} \end{array}$$

where (x, y) is any coordinate, $f(x, y)$ is a grayscale intensity at (x, y) , and $g(x, y)$ is a binary intensity (0 indicates black and 1 indicates white).

2.2.2 Major Axis Length

Major axis length is used to determine the size of an object contains in a binary image. This length is calculated by drawing an ellipse to perfectly fit a binary object (white region) and return the ellipse's length in pixel as the major axis length. Figure 5 illustrates the major axis of an ellipse.



CHULALONGKORN UNIVERSITY
Figure 5 Major axis
which is shown in red line

2.2.3 K-Mean Clustering

One of the most popular clustering techniques is called k-mean clustering which was first proposed by Stuart Lloyd in 1957, but was published in 1982 [19]. The concept of k-mean clustering is to first random by select k points and later calculate a distance between each given dataset to those k random points whether each data point in the dataset belongs to or closet to which k random point. After point assignment, the dataset is then separated into k groups. A new centroid of each group is calculated based on data points within its group and then substitutes

its prior centroid. Next, the process of assigning points to the closet k points or centroids and centroid recalculation is repeated again until the centroids are constant. Figure 6 represents k-mean clustering steps.

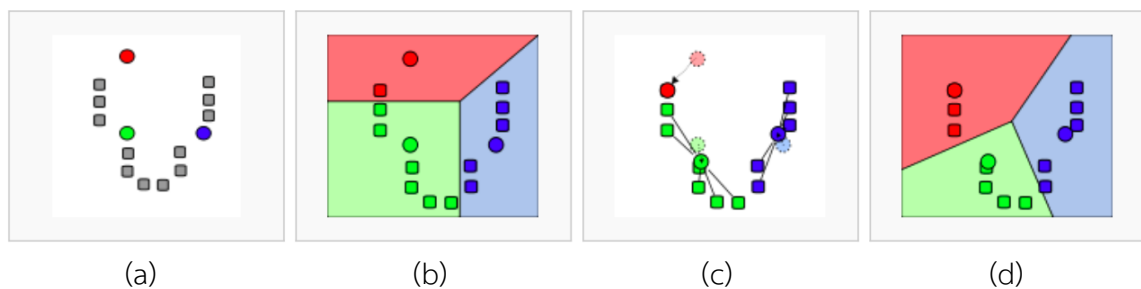


Figure 6 K-mean clustering

(a) initial k random points ($k=3$, presented in color),

(b) assign data to closet k random points,

(c) recalculate centroids of each clusters, and

(d) iterate until centroids are stable

(http://en.wikipedia.org/wiki/K-means_clustering)

2.2.4 Polar Coordinate System

Polar coordinate system is a two-dimensional system referring as (radius, theta) coordinate whose center or origin is at the center of a picture. Most of the polar coordinate system starts its system at the horizontal line on the right hand side and rotates counter clockwise. Thus, theta is an angle between the point and the horizontal line that points to the right whereas the radius is the distance from the origin to that point. The reference of a polar coordinate system is shown in Figure 7.

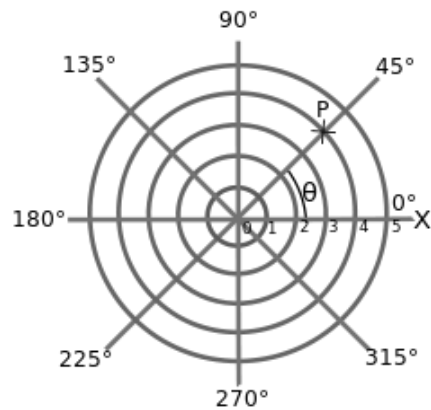


Figure 7 Polar coordinate system

(http://en.wikibooks.org/wiki/Geometry_for_Elementary_School/Polar_coordinate_system)

2.2.5 Density-Based Spatial Clustering of Applications with Noise (DBSCAN)

Ester, Kriegel, Sander and Xu proposed an idea of data clustering based on data density called Density-based spatial clustering of applications with noise or DBSCAN [20]. DBSCAN has two major parameters to be considered; ϵ (eps) and minPts. Eps represents the distance within a cluster while minPts is the minimum number of points to form a cluster. As depicted in Figure 8, when starting DBSCAN at any point A and searching for points within ϵ distance, any particular point that can be reachable, will be assigned to cluster A. After the search, if the number of points in a cluster is less than minPts, this cluster is marked as noise. On the contrary, if there are sufficient points in the cluster; i.e. greater than or equal to minPts, this forms a cluster.

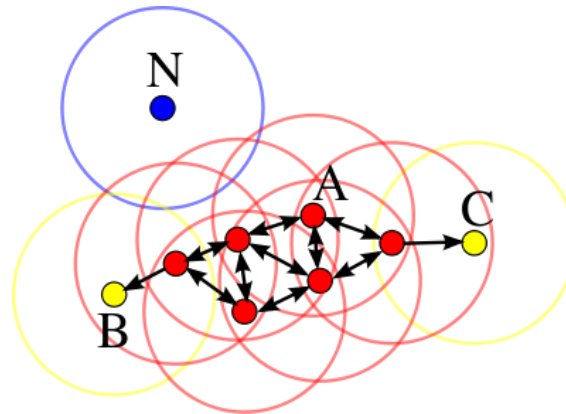


Figure 8 DBSCAN

where A represents a starting point of a cluster that has B and C as density-reachable points; thus they formed a cluster, while N is recognized as noise

(<http://en.wikipedia.org/wiki/DBSCAN>)

2.2.6 Second Order Derivatives

Second order derivative is used to measure rate of change of data by considering three points at a time. Eq.(1) below illustrates second order derivative calculation.

$$f''(x) = f(x-1) + f(x+1) - 2f(x) \quad (1)$$

where x represents any pixel,
 $f(x)$ represents intensity of that pixel, and
 $f''(x)$ is the second order derivative at considering pixel x .

If there is a high change on the value at x , the second order derivative return extremely high negative value, whereas high positive value of second order derivative indicates low change in x . Zero second derivative refers to no change in x , $x-1$ and $x+1$.

2.2.7 Cubic Spline Interpolation

Spline interpolation is an interpolation in piecewise polynomial fashion by sectioning predefined data into subsets and interpolating using lower-degree

polynomial [21]. Therefore, spline interpolation can produce less error comparing to piecewise polynomial interpolation due to its lower order. Cubic or third-order spline interpolation is unlike third degree of polynomial interpolation that considers the whole dataset. It uses polynomial of degree three to interpolate over each interval by considering a pair of data to form spline functions and solve for their coefficients under an agreement that the functions must pass through the points and their first and second order derivatives should correlate with their in-between points. The difference between cubic spline interpolation and interpolating cubic is shown in Figure 9.

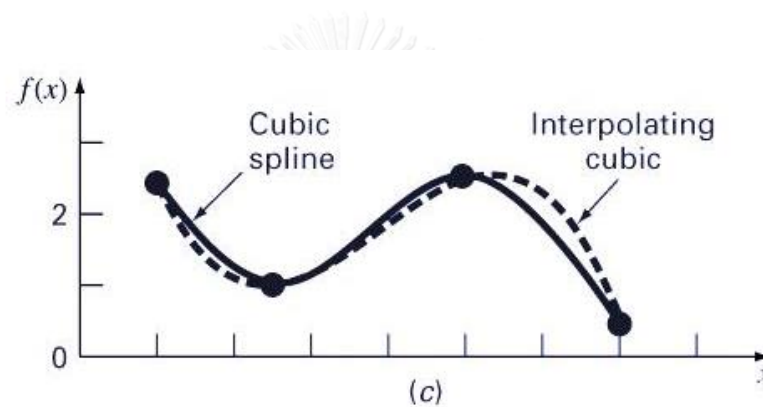


Figure 9 Comparison between cubic spline and interpolating cubic
<http://www3.nd.edu/~msen/Teaching/NumMeth/BookSlides/Chapter16rev1.ppt>

2.2.8 Entropy

Entropy is a textural measurement of randomness of a grayscale image calculated by Eq.(2) [22].

$$Entropy = - \sum (p .* \log_2 (p)) \quad (2)$$

where \mathbf{p} is a column vector of the number of pixels of each gray level where its row represents gray levels and the size of \mathbf{p} is equal to the number of gray levels.

2.2.9 Gray-Level Co-Occurrence Matrix (GLCM)

One of several useful statistical textural measurements is known as gray-level co-occurrence matrix, which is used to measure an occurrence of pixel i in accordance with pixel j in a specified direction such as a sample image depicted in Figure 10. Suppose that there is an 8-level image as illustrated in Figure 10(a), GLCM of size 8×8 is constructed corresponding to image levels as shown in Figure 10(b). A value in (i,j) pixel of GLCM indicates the number of occurrence of i related to j in a specified direction, in this case, the direction of 1-pixel to the right. As in pixel $(1,1)$ (circled in red) in Figure 10(a), the number of occurrence of 1 followed by 1 to the right can only be seen once. Therefore, 1 is put in $(1,1)$ of GLCM in Figure 10(b). Additionally, the value of $(1,2)$ is equal to 2 because there are two occurrences of 1 following by 2 to the right.

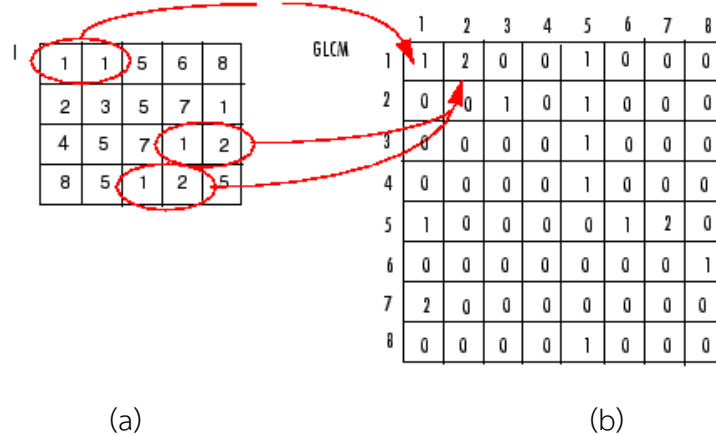


Figure 10 Gray-level co-occurrence matrix (GLCM)

(a) a considered image (b) its GLCM

(<http://www.mathworks.com/help/images/ref/graycomatrix.html>)

Moreover, there are four features that can be extracted from GLCM, which are contrast, correlation, energy, and homogeneity.

Contrast: the measurement of contrast of intensity between a pixel and its neighbor throughout an image or known as variance and inertia. Zero contrast

suggests a constant image. The equation used to calculate contrast is shown in Eq.(3).

$$\sum_{ij} |i - j|^2 p(i, j) \quad (3)$$

where (i, j) represents any value in GLCM, and $p(i, j)$ is the value at (i, j) of GLCM.

Correlation: the measurement of intensity correlation between a pixel and its neighbor throughout an image. The range of correlation is between -1 and 1 where NaN suggests a constant image. The correlation equation is demonstrated in Eq.(4).

$$\sum_{ij} \frac{(i - \mu_i)(j - \mu_j)p(i, j)}{\sigma_i \sigma_j} \quad (4)$$

where μ_i, μ_j are the means of probability matrix GLCM along row wise i and column wise j , and $\sigma_i \sigma_j$ are the standard deviations of probability matrix GLCM along row wise i and column wise j .

Energy: the sum of square of pixels in GLCM or known as measurement of uniformity of energy, whose values are between 0 and 1 where one indicates a constant image. The energy equation is described in Eq.(5).

$$\sum_{ij} |i - j|^2 \quad (5)$$

where i, j represent row and column of GLCM, respectively.

Homogeneity: the measurement of the distribution of closeness of pixels in GLCM to diagonal of GLCM. The homogeneity range is between 0 and 1 where 1 shows a diagonal GLCM. The formula of homogeneity is illustrated in Eq.(6).

$$\sum_{ij} \frac{p(i,j)}{1+|i-j|} \quad (6)$$

where (i,j) represents any value in GLCM, and $p(i,j)$ is the value at (i,j) of GLCM.

2.2.10 Ray Tracing

Ray tracing in computer graphic is described as a method to generate an image by observing the ray passes through a spatial image and rendering effects of ray on 3D objects [23]. Additionally, ray tracing can be applied in image processing by sampling image intensity on a particular direction of ray and plotting the path on a 2-dimensional plane. This plot could be used to identify a pattern of an image, especially when additional rays have been integrated in order to scan more sampling in more directions.

2.2.11 Zero Crossing

In mathematics, zero crossing is normally used to recognize a change of a sign of a function from negative to positive or vice versa [24]. It is also useful in image processing in term of texture analysis by capturing high changes in intensities of image texture. Suppose that a function represents intensity values, thus, the more the number of crossing through zero line, the more fluctuated of image patterns which could probably refer to heterogeneity.

2.2.12 Artificial Neural Networks (ANNs)

Artificial neural network is a computational model to mimic functions of a brain by processing multiple data in non-linear manner and being able to learn by adjusting data weights [25]. ANNs structure is an interconnection of nodes or neurons based on three major layers—input layer, hidden layer, and output layer—as illustrated in Figure 11. It composes of adaptable weights between each node pair of different layers and multiple learning algorithms such as back propagation method.

The common type of ANNs is three-layered feed forward ANNs with back propagation learning algorithms, which starts a process by feeding data into input layer, follows by combining random weights with these inputs, forwarding the combination to the hidden layer, propagating back the errors to adjust the weights accordingly, and then repeating the whole steps again until reaching the output layer with minimum error at the highest accuracy. Actually, in machine learning, input data should firstly be separated into three groups—training group which is used to construct a network model, validation group which helps to verify and stop the model, and test group which is used to provide independent dataset for measuring performance—before feeding into a network. Therefore, more data sample provided or additional data preprocessing could help increasing the accuracy. Additionally, increasing in the number of hidden layers not only yields higher accuracy, but also supports more complex processing. However, it may cause over fitting problem—a problem occurs when high accuracy of training data is achieved but low accuracy presented in test data.

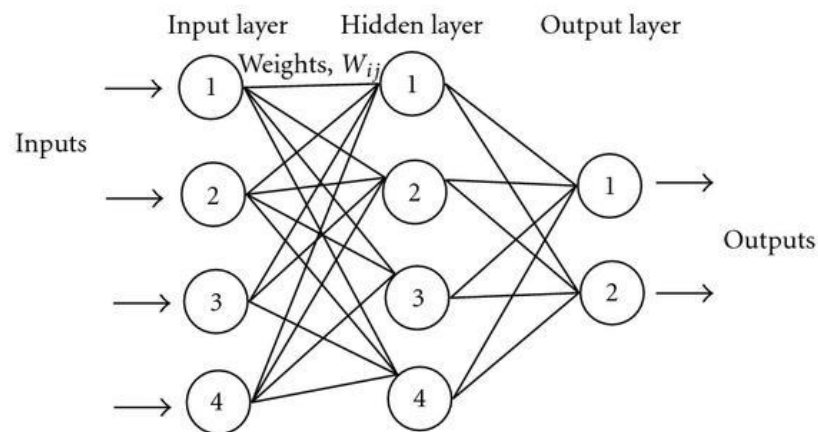


Figure 11 Configuration of feed-forward artificial neural networks

(<http://www.hindawi.com/journals/aai/2011/686258/fig1/>)

2.2.13 Cross Validation

In classification, data are mostly separated into two disjoint sets of training and testing (or probably three sets including validating set to tune the train model)

where training set is used to create a classification model and test set is used to obtain a test accuracy of the model. However, to split data into a single training and test set known as hold-out method can yield inconsistent accuracy. K-fold cross validation is performed to overcome this problem by separating data into non-overlapped k sets, constructing k experiments, holding k^{th} group of data to be the test data and using the rest of data to train the model. There will be k independent models used to calculate an average cross validation test accuracy. The model with the highest test accuracy will be selected as the representative model. Figure 12 shows 4-fold cross validation. Therefore, cross validation helps guarantee that data are used as both training and test data. Additionally, the common number of fold is 10.

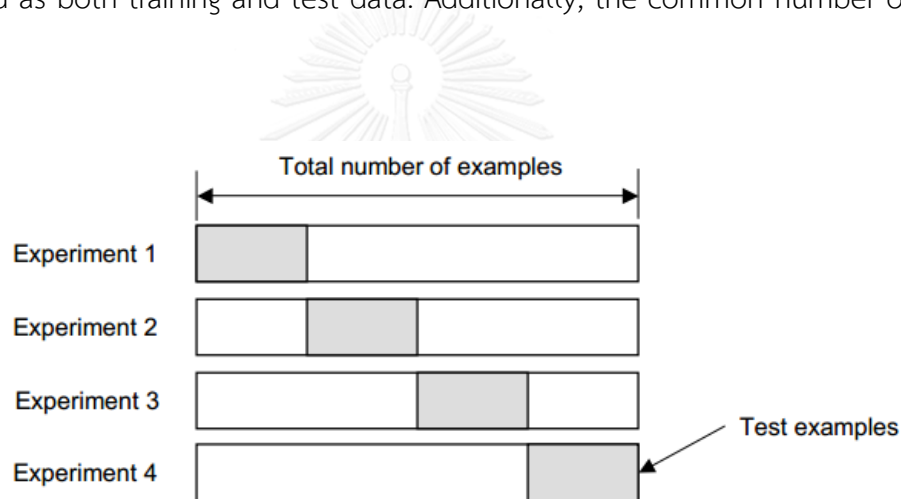


Figure 12 Cross validation

(http://research.cs.tamu.edu/prism/lectures/iss/iss_l13.pdf)

2.2.14 Confusion Matrix

Confusion matrix or contingency table is well-known in machine learning [26]. It helps to summarize the error and performance of supervised learning by showing both correct and incorrect classification. The column of confusion matrix represents the expectation or predicted class whereas its row represents the actual data or test outcome as shown in Figure 13. There are multiple terms that may be necessary for further contents, listed below:

True positive (TP): The number of correct prediction as true

True negative (TN): The number of correct prediction as false

False positive (FP): The number of incorrect prediction that first predict as false but the actual outcome is true

False negative (FN): The number of incorrect prediction that first predict as true but the actual outcome is false

Sensitivity: The ability of test to correctly predict which can be calculated by:

$$\text{Sensitivity} = \frac{TP}{TP + FN} \quad (7)$$

Specificity: The ability of test to correctly exclude the false which is determined by:

$$\text{Specificity} = \frac{TN}{TN + FP} \quad (8)$$

Accuracy: The ratio of correct prediction including true positives and true negatives obtained during classification which is described below:

$$\text{Accuracy} = \frac{TP + TN}{TP + FP + FN + TN} \quad (9)$$

		Condition (as determined by "Gold standard")		
		Condition positive	Condition negative	
Total population				Prevalence = $\frac{\Sigma \text{Condition positive}}{\Sigma \text{Total population}}$
Test outcome	Test outcome positive	True positive	False positive (Type I error)	Positive predictive value (PPV, Precision) = $\frac{\Sigma \text{True positive}}{\Sigma \text{Test outcome positive}}$
	Test outcome negative	False negative (Type II error)	True negative	False omission rate (FOR) = $\frac{\Sigma \text{False negative}}{\Sigma \text{Test outcome negative}}$
Positive likelihood ratio (LR+) = TPR/FPR		True positive rate (TPR, Sensitivity, Recall) = $\frac{\Sigma \text{True positive}}{\Sigma \text{Condition positive}}$	False positive rate (FPR, Fall-out) = $\frac{\Sigma \text{False positive}}{\Sigma \text{Condition negative}}$	Accuracy (ACC) = $\frac{\Sigma \text{True positive} + \Sigma \text{True negative}}{\Sigma \text{Total population}}$
Negative likelihood ratio (LR-) = FNR/TNR		False negative rate (FNR) = $\frac{\Sigma \text{False negative}}{\Sigma \text{Condition positive}}$	True negative rate (TNR, Specificity, SPC) = $\frac{\Sigma \text{True negative}}{\Sigma \text{Condition negative}}$	

Figure 13 Confusion matrix

(http://en.wikipedia.org/wiki/Confusion_matrix)

CHAPTER III

METHODOLOGY

There are five steps in our proposed methodology as illustrated in Figure 14, which are preprocessing, boundary detection, best frame selection, feature extraction, and classification.

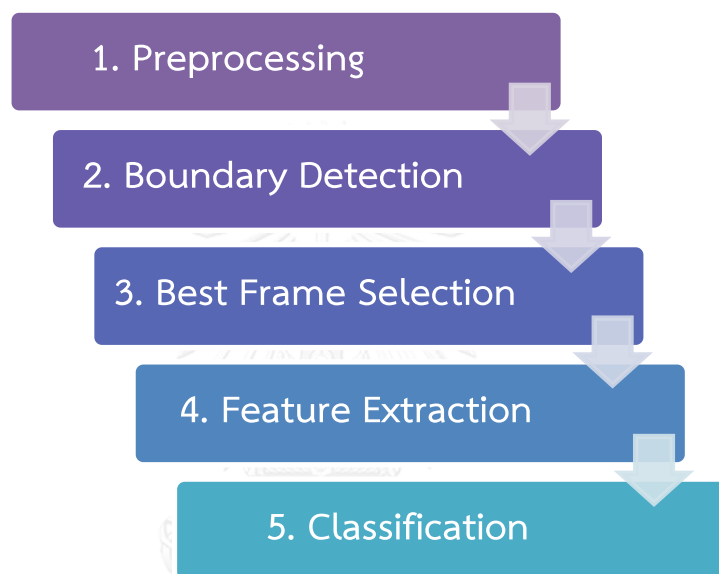


Figure 14 Proposed methodology

1. Preprocessing

The input comes in the form of EBUS video, which composes of several frames or images. Each frame is required to be converted into grayscale and to crop out irrelevant portion such as metadata written on the screen, leaving only an actual image to be processed as shown in Figure 15.

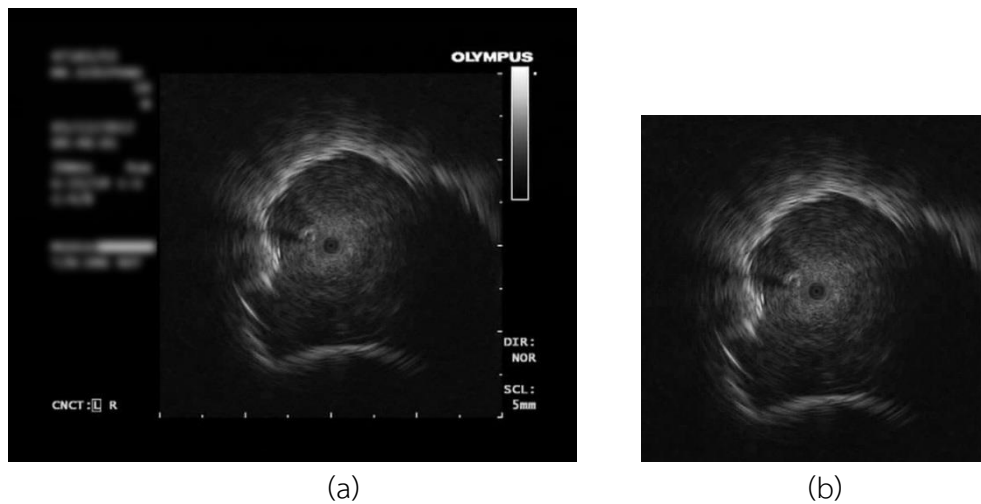


Figure 15 Preprocessing image

(a) before and (b) after converting to grayscale and cropping

However, not all images contain lesion texture. There are some blank frames with no texture which appears black as shown in Figure 16(a)—or frames with solely artifacts as seen with a few white pixels as shown in Figure 16(b).

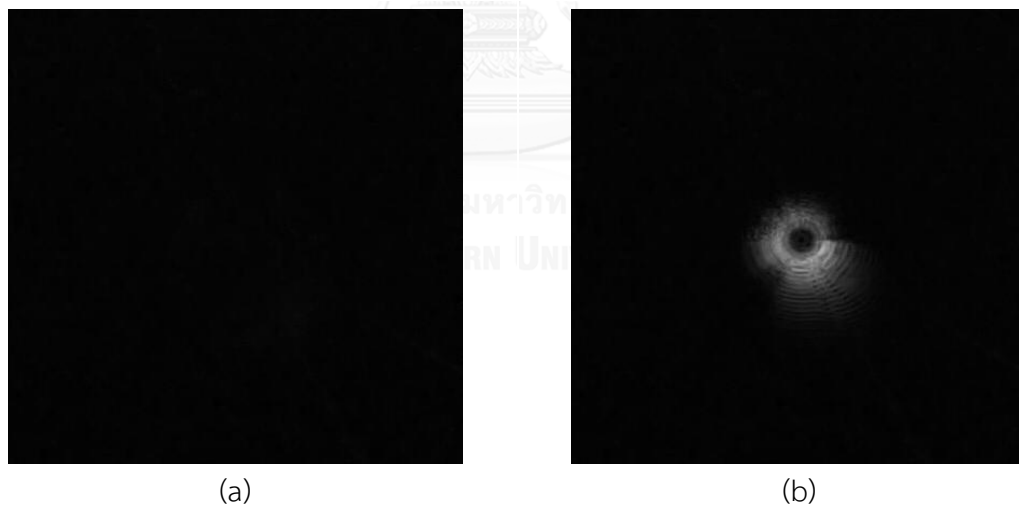


Figure 16 Images to be eliminated

(a) an image with no texture, (b) an image with artifacts

Since texture appears as hyperechoic area or lighter area, the elimination of a blank frame can be done by converting a grayscale image into a binary image as illustrated in Figure 17, and checking further whether these white pixels should be

considered as a group of texture or not. Thus, any binary image, whose major axis length of white area is less than the threshold, is deleted.

Additionally, a set of EBUS images may contain duplicated frames. Pixel-by-pixel absolute difference of intensity of every consecutive frame is measured according to Eq.(10). The differences are then clustered using k-mean clustering into a group of high difference to be maintained and a group of low difference to be omitted.

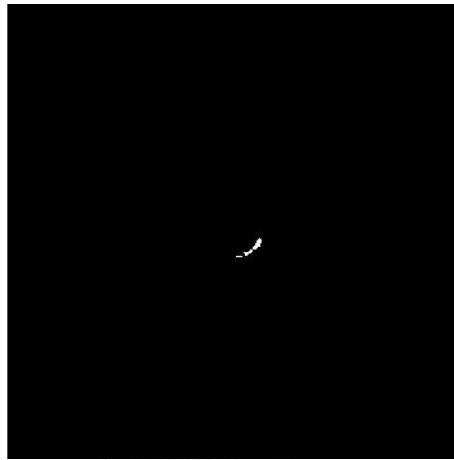


Figure 17 Grayscale to binary image of the image in Figure 16(b)

$$diff(i) = \sum_{y=1}^n \sum_{x=1}^m |im_i(x, y) - im_{i-1}(x, y)| \quad (10)$$

where i is the i^{th} frame of EBUS video,
 $i - 1$ is a frame prior to i^{th} frame of EBUS video,
 $diff(i)$ is a pixel-by-pixel absolute difference between i^{th} and $i-1^{\text{th}}$ frame,
 $im_i(x, y)$ is an intensity at (x, y) of i^{th} frame, and
 m, n are the height and width of EBUS frame.

2. Boundary Detection

After the preprocessing step, the remaining frames, which may best describe the patient lesion type, are obtained. Nonetheless, there is still a plenty of frames to

be considered. Actually, only a single EBUS frame is adequate to identify the result according to prior studies that required manpower to select the best frame and categorize EBUS characteristics. As such, we need to automatically select the best representative frame to further undergo feature extraction. The key to select the best frame is to firstly perform boundary detection since the best frame may contain the largest proportion of lesion, result in the largest area of boundary.

Moreover, boundary detection is useful to identify a region of interest. While operating feature extraction, we should omit the area outside the lesion, which might interfere the result of feature calculation. The following steps are introduced in performing boundary detection for each EBUS frame.

2.1 360-Degree Iterative Maximum Intensity Detection

Each pixel of an image is transformed from Cartesian coordinates (x, y) into polar coordinates (radius, theta) by firstly assigning the central pixel of an image as the origin of the polar system. Then, an image is divided into 360 sectors according to the degree of theta. Regarding echogenicity of the boundary, the actual boundary tends to have hyperechoic characteristics. Thus, a pixel with maximum intensity of each sector is selected as a boundary candidate. If there are two or more pixels having the same maximum intensity, the innermost pixel or the pixel with the shortest radius is selected. After the candidate pixels of all sectors are obtained, the new origin of the polar system is calculated according to these candidates. Next, the process of detecting a pixel with maximum intensity of each sector is iterated again until the new origin is stable or is the same as the previous origin. The reason behind moving polar origin is that not every bronchoscopy can obtain a video with a lesion at the center since it depends on the location of the lesion within the lung whether a bronchoscope can go within or be adjacent to a lesion. Hence, samples of final boundary candidates are illustrated as yellow dots in Figure 18.

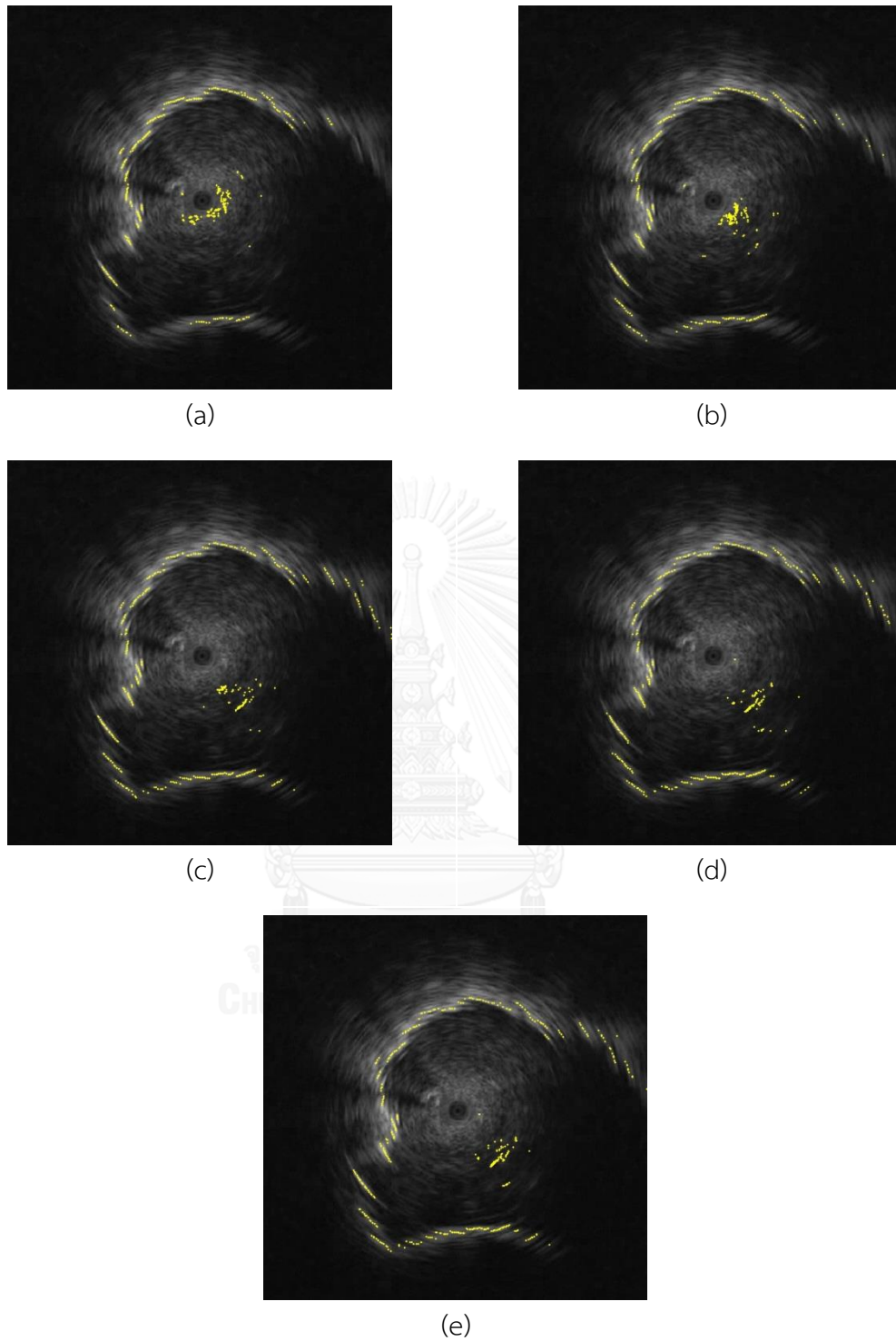


Figure 18 360-Degree iterative maximum intensity detection
(a)-(e) results of 360-degree iterative maximum intensity detection of round 1-5,
respectively

2.2 Density-Based Spatial Clustering of Applications with Noise (DBSCAN)

Iteration

After all candidate pixels are acquired, these pixels have to be identified whether they are part of a lesion boundary or not by using Density-Based Spatial Clustering of Applications with Noise (DBSCAN), as a clustering method to divide them into clusters. Assuming that the minimum number of points to form a cluster is 10; otherwise, they are considered as noise. Each cluster forms a boundary segment. By heuristic evaluation, 10 pixels are small enough to separate coordinates into consecutive boundary segments, and large enough to consider a high density group of coordinates as another segment, but not to recognize them as noise. Then, statistical data of individual clusters, including standard deviation of segments' radius, are calculated. DBSCAN is iterated over a cluster that has a standard deviation of radius higher than 10. If all clusters have their standard deviation of radius below 10, they are highly coherent which cannot be subdivided any further. Therefore, this process terminates. Figure 19 depicts a sample result of iteration over DBSCAN. Different color distinctively labels the clusters.

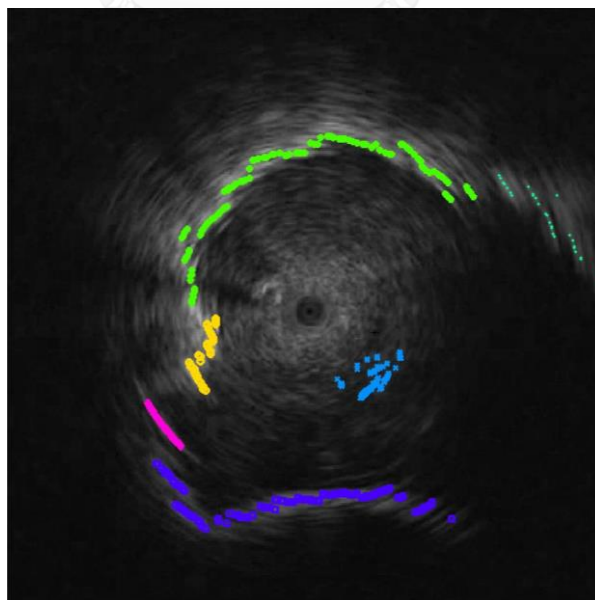


Figure 19 Result after DBSCAN iteration where clusters are separated by colors

2.3 Elimination by Second Order Derivative and Global Average Intensity

In order to eliminate clusters that do not belong to a boundary, instead they are actually noise with high intensity, second order derivatives of local mean radius of each cluster is used and can be calculated according to Eq.(11). If there is any cluster whose second order derivative of local mean radius is higher than the mean radius among three considering consecutive clusters and also has the local mean intensity lower than the global mean intensity, it will be removed. The result after performing elimination by second order derivative is shown in Figure 20.

$$f''(x) = f(x - 1) + f(x + 1) - 2 f(x) \quad (11)$$

where $x = 1, 2, \dots, n$ clusters,
 n is the number of clusters arranged by theta,
 $f(x)$ is the average radius of x^{th} cluster,
 $f(x - 1)$ is the average radius of $(x-1)^{\text{th}}$ cluster,
 $f(x + 1)$ is the average radius of $(x+1)^{\text{th}}$ cluster,
 $f''(x)$ is the second order derivative of x^{th} cluster.

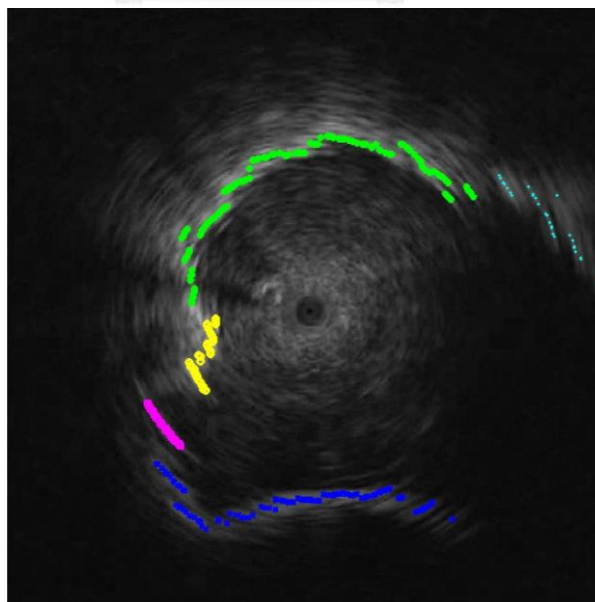


Figure 20 Result of elimination by second order derivatives and average intensity

2.4 Polar Coordinate System Origin Adjustment

After eliminating noise, the origin of polar system is then relocated back to the image center. Therefore, the radius and theta of the remaining polar coordinates should be recalculated according to the new origin in order to be consistent across all data.

2.5 Cubic Spline Interpolation

Finally, all of the pixels are reconnected to each other while the missing representative pixels are estimated by cubic spline interpolation with theta (x) and radius (y) as the input data. Consequently, a spline function is used to estimate the unknown radii to match with the given thetas in a specific range of -180 to 180 degree. The result of this process is demonstrated in Figure 21.

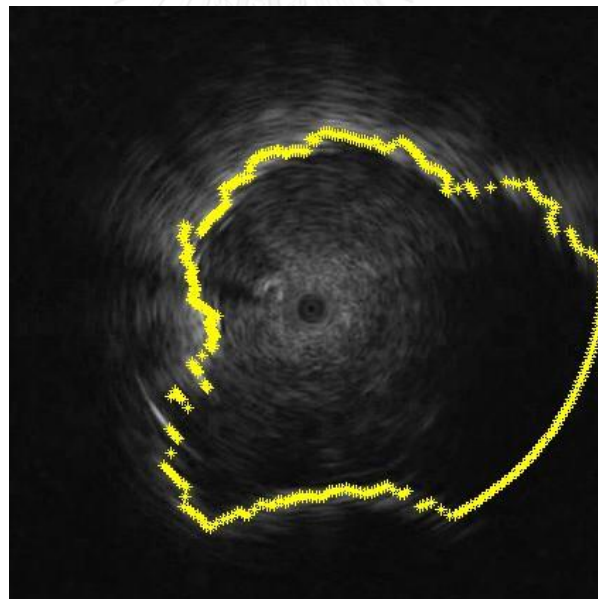


Figure 21 Result after spline interpolation

3. Best Frame Selection

Since EBUS is recorded in term of video, which are still composed of several frames or images after preprocessing, an issue arises during selecting the best frame to represent patient's lesion texture.

When performing boundary detection, some parameters are needed to be recorded in order to operate the best frame selection such as locations of interpolating boundaries and the number of incomplete boundary sectors before interpolation. Best frame in this case is selected based on two properties: the largest proportion of area of minimum bounding box of boundaries versus the whole image area, and the highest ratio between the number of boundary sectors before interpolation and 360—a maxima of boundary sectors due to 360-degree boundary division. Eq.(12) demonstrates the criteria for best frame selection.

$$best\ frame = \max\left(\frac{bbArea}{image\ area} + \frac{\#bBefore}{360}\right) \quad (12)$$

where *image area* is the number of pixels in the image.
bbArea is bounding box area, and
#bBefore is the number of boundaries before interpolation.

4. Feature Extraction

Next, the best frame of each data sample is processed. The image is then normalized to the range [0, 255] as depicted in Figure 22. A logical mask is constructed according to the detected boundary by filling the area inside the boundary with one and filling with zero everywhere else as shown in Figure 23. This mask is used to scope the region of interest (ROI) of the image.

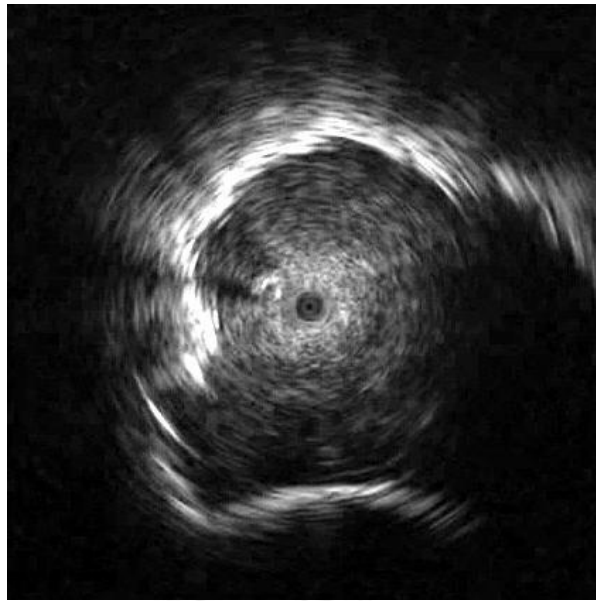


Figure 22 Result after intensity normalization

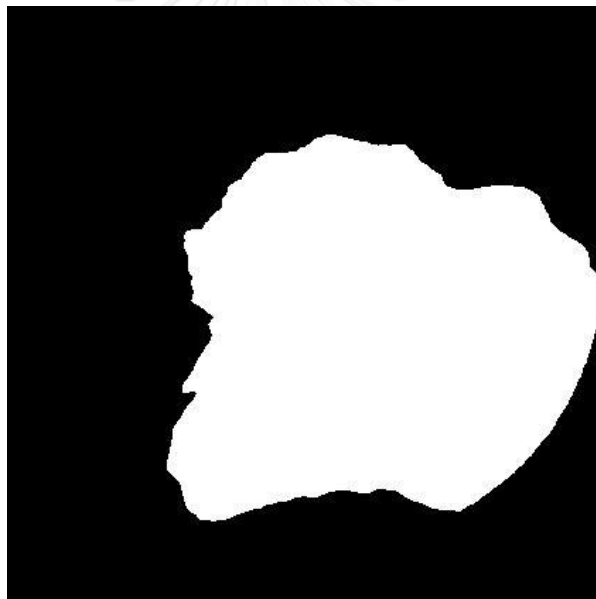


Figure 23 Logical mask

After that, the best frame is overlaid with the mark (shown in Figure 24) and cropped according to a minimum bounding box of the mask to eliminate uninterested black area, as demonstrate in Figure 25, in order to further extract features; for instance, entropy, contrast, correlation, energy, and homogeneity. With the help of gray-level co-occurrence matrix (GLCM), it is easy to calculate contrast, correlation, energy and homogeneity. By specifying an offset or a distance between

the pixel of interest and its four neighbors at four different angles which are 0, 45, 90, and 135-degree, can result in four different GLCMs for four features. Furthermore, we suggest another feature to measure homogeneity called Adaptive Ray Tracing. This method composes of two steps as follows:

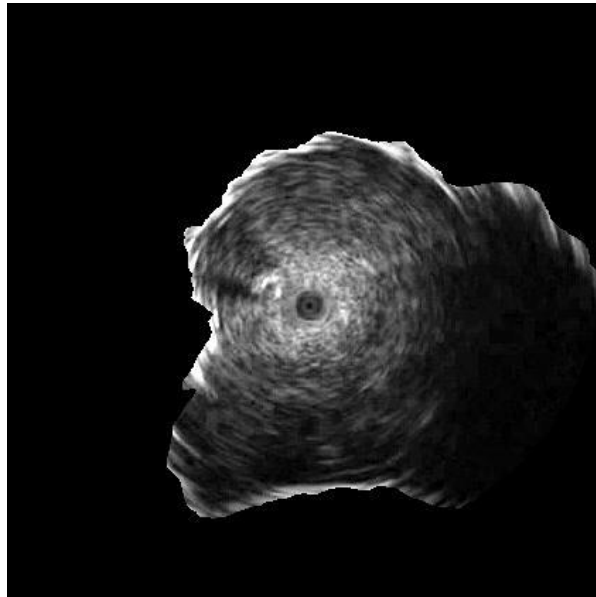


Figure 24 Best frame overlaid with a mask

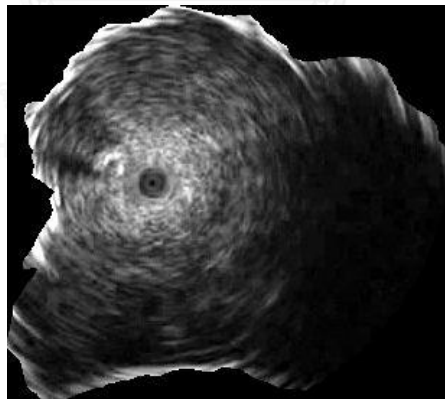


Figure 25 After crop the image in Figure 24

4.1 Adaptive Ray Tracing

Adaptive ray tracing is constructed by drawing 4-direction lines through the center of the image which contains the central black hole or a probe. These lines consist of horizontal line (0-degree), vertical line (90-degree), and two diagonal lines (45 and 135-degree). The intensities along the line are recorded in an array to be

plotted as a graph of array index versus intensity as depicted in Figure 26. As the result, four graphs in Figure 27 represent the intensities collected by each illustrated line.

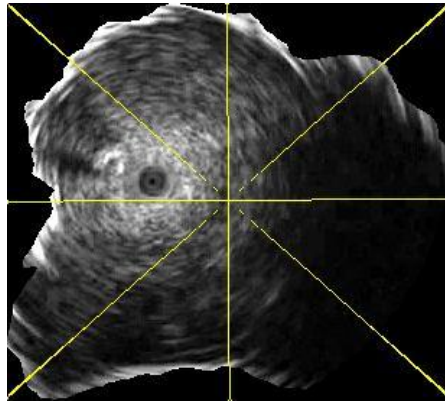
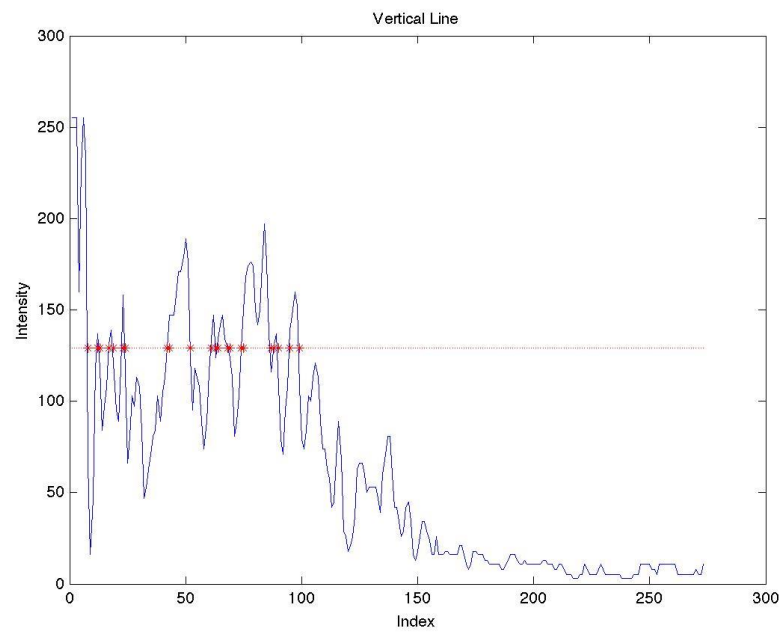
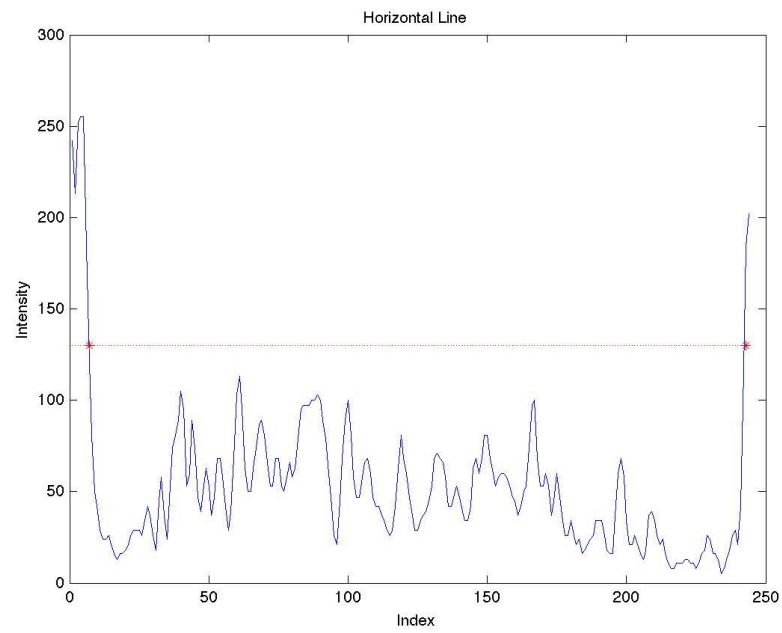


Figure 26 4-Direction of ray tracing through an image

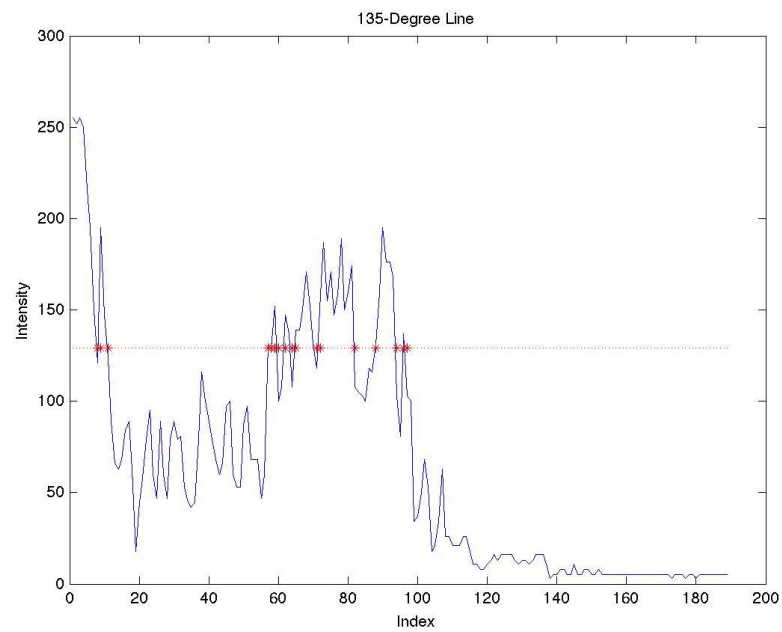
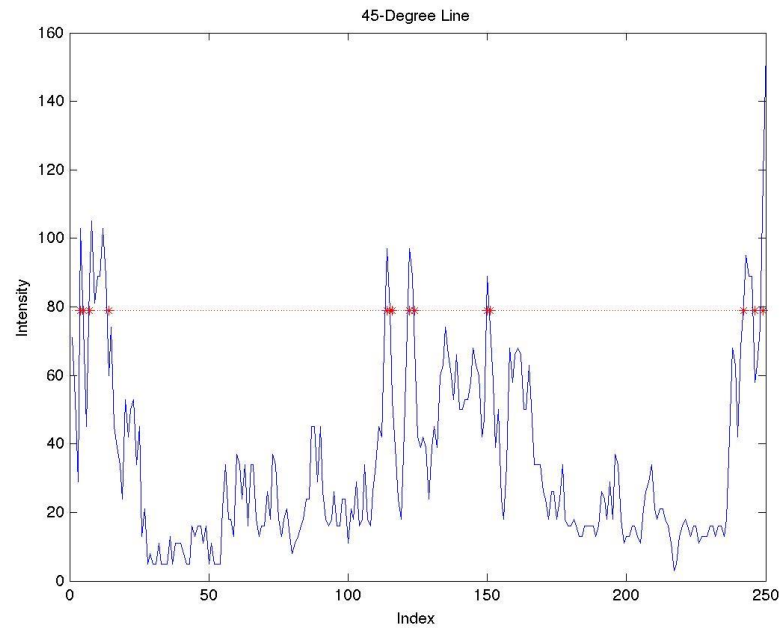
4.2 Crossing Count

Zero-crossing is a process which counts the number of times in which points on each line from ray tracing pass through a horizontal line of zero in order to estimate the fluctuation of a line. On the other hand, we develop our own idea by setting a crossing level at average intensity as shown in Eq.(13), since the graph that we mention about is a record of intensity levels. Crossing count is performed to count the number of times that the intensities pass through the crossing level. In order to measure the lesion echogenicity and to classify whether it is homogeneous or heterogeneous pattern, the smoothness of the graph is needed to be calculated. From the assumption that the intensities along the tracing path must be uniform for homogeneous pattern, the intensity along the line could show fewer changes than heterogeneous pattern. Thereby, the higher number of the crossing count, the more chaotic of the graph is inversely proportional to the graph smoothness. An example of 4-direction ray tracing and its crossing count are demonstrated in Figure 27.

$$\text{Crossing level} = \text{mean intensity} \quad (13)$$



(b)



(d)

Figure 27 4-Direction ray tracing and its crossing line
 where blue line indicates ray tracing, red line indicates its crossing level whereas red
 asterisks represent crossing points (a) 0-degree (b) 90-degree (c) 45-degree
 (d) 135-degree ray tracing

Additionally, the number of boundary sectors before interpolation (*#bBefore*) available in the process of best frame selection is also involved in the feature list due to its properties that may represent continuous/non-continuous margin characteristics.

Furthermore, continuous/non-continuous margin is naturally defined by the number of sweeping angles of the boundary sector before interpolation. Thus, the longest consecutive non-interpolated boundary sectors are counted in number to be presented as another feature.

The following table (Table 1) describes 23 features that will be further applied for classification.



Table 1 Feature list for classification

No.	Feature
1	Entropy
2	Contrast at 0-degree
3	Contrast at 45-degree
4	Contrast at 90-degree
5	Contrast at 135-degree
6	Correlation at 0-degree
7	Correlation at 45-degree
8	Correlation at 90-degree
9	Correlation at 135-degree
10	Energy at 0-degree
11	Energy at 45-degree
12	Energy at 90-degree
13	Energy at 135-degree
14	Homogeneity at 0-degree
15	Homogeneity at 45-degree
16	Homogeneity at 90-degree
17	Homogeneity at 135-degree
18	Ray Tracing and Crossing Count at 0-degree
19	Ray Tracing and Crossing Count at 45-degree
20	Ray Tracing and Crossing Count at 90-degree
21	Ray Tracing and Crossing Count at 135-degree
22	Number of Boundary Sectors before Interpolation
23	Number of Longest Consecutive Boundary Sectors before Interpolation

5. Classification

Data are classified using multiple-layer feed-forward artificial neural networks (ANNs) with back-propagation algorithm of 10 hidden layers and 10-fold cross validation. Figure 28 illustrates the network model.

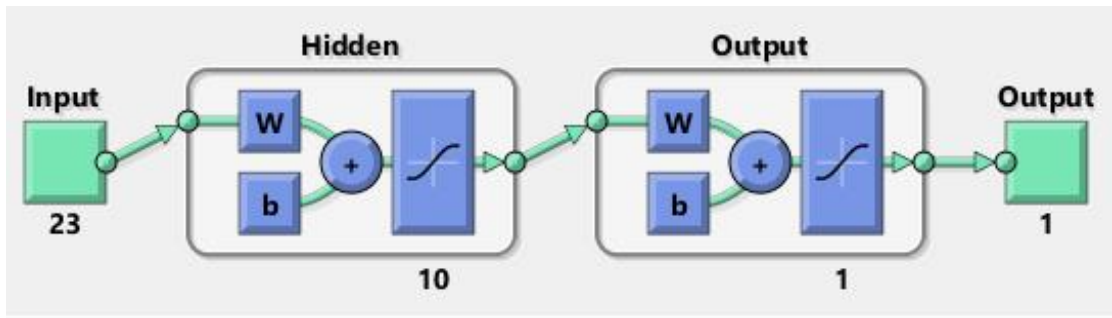


Figure 28 Network model



CHAPTER IV

EXPERIMENTAL RESULTS

Input data are video files, which were recorded during endobronchial ultrasonography at Phramongkutklo Hospital, Bangkok, Thailand during 2011-2013. The data are composed of 31 samples of benign and 65 samples of malignant lesions, results in 96 videos in total as illustrated in percent in Figure 29. Additionally, the video file format is MPEG-1 with a dimension of 576 x 720 pixels or 288 x 352 pixels, which was captured at frame rate of 25 frames per second.

Lesion type

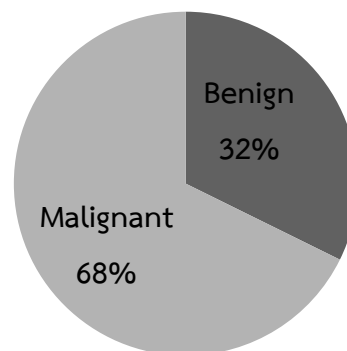


Figure 29 Proportion of each lesion type

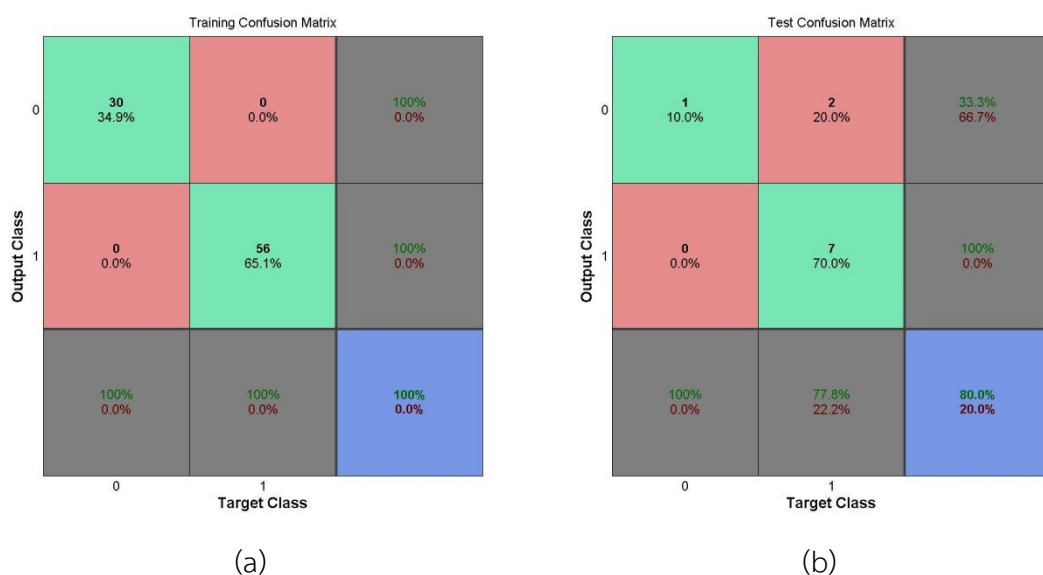
The histopathology results of the patients which were confirmed after reviewing patient lesions under microscope, are set as the ground truth data for evaluating the proposed method. Test accuracy of each fold is illustrated in Table 2, which yield an average cross validation test accuracy of 66.67%. The best model, which achieved maximum test accuracy at 80%, is the model of third fold.

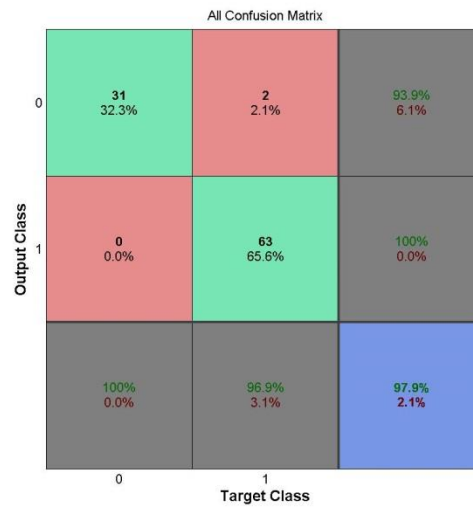
Table 2 Test accuracy of every fold of 23 features

i^{th} Fold										Average
1	2	3	4	5	6	7	8	9	10	
70	66.67	80	70	60	77.78	55.56	60	66.67	60	66.67

Figure 30 (a-c) illustrate the confusion matrices of training, test, and all data, which are classified by the best model. Mostly in clinical, the term “positive” usually refers to a condition of having a disease or having a cancer cell (malignant) in this case, whereas the term “negative” refers to a condition of rejecting the disease or not having a cancer cell (benign). Therefore, the confusion matrix shown here is a table plotted between the target results obtained from the doctors represented in columns of malignant (positive) and benign (negative), and the output results obtained from the best classification model represented in rows of malignant (positive) and benign (negative).

For 86 training data in Figure 30(a), the best model performed 100% correct classification. On the other hand, for the 10 test data shown in Figure 30(b), the number of true positive or the number of lesions targeted as malignant and the output as malignant is 7 while the number of true negative or the number of lesions targeted as benign and the output as benign is 1, result in 80% correct classification. For the incorrect classification, the number of false positive or the number of lesions targeted as benign and the output as malignant is 0, whereas the number of false negative or the number of lesions targeted as malignant and the output as benign is 2. The test sensitivity, specificity and accuracy are 77.78%, 100% and 80%, respectively.





(c)

Figure 30 Confusion matrices of the best model of 23 features with (a) training (b) test (c) all data

For the overall data represented in Figure 30(c), the whole dataset achieves percentages of true positive, false positive, true negative and false negative, at 65.6, 0, 32.3 and 2.1, respectively, resulted in 97.9% accuracy with 96.9% sensitivity and 100% specificity.

The final weights of every feature after weight adjustment in neural networks are demonstrated in Table 3 arranged by their ranks in the last column. Weight ranks are calculated by the average of the absolute weights in every neural network layer of each feature. Entropy, ray tracing and crossing count at 180-degree, homogeneity at 45-degree, ray tracing and crossing count at 45-degree, homogeneity at 0-degree, correlation at 135-degree, ray tracing and crossing count at 0-degree, correlation at 180-degree, number of boundary sectors before interpolation, correlation at 45-degree are the top 10 features among 23 features.

Table 3 Weight rank of 23 features

No.	Feature Title	Rank
1	Entropy	1
19	Ray Count at 180-degree	2
16	Homogeneity at 45-degree	3
20	Ray Count at 45-degree	4
14	Homogeneity at 0-degree	5
9	Correlation at 135-degree	6
18	Ray Count at 0-degree	7
7	Correlation at 180-degree	8
22	Boundary Sectors before Interpolation	9
8	Correlation at 45-degree	10
5	Contrast at 135-degree	11
4	Contrast at 45-degree	12
23	Longest Consecutive Boundary Sectors	13
2	Contrast at 0-degree	14
21	Ray Count at 135-degree	15
10	Energy at 0-degree	16
12	Energy at 45-degree	17
11	Energy at 180-degree	18
6	Correlation at 0-degree	19
17	Homogeneity at 135-degree	20
3	Contrast at 180-degree	21
13	Energy at 135-degree	22
15	Homogeneity at 180-degree	23

CHAPTER V

DISCUSSIONS AND CONCLUSION

As depicted in Table 3, the proposed features namely ray tracing and crossing count at 180-degree, 45-degree, 0-degree and number of boundary sectors before interpolation are at 2, 4, 7 and 9th rank, respectively are probably important features to differentiate between benign and malignant lesions. After considering weight rank table, energies at any direction seem to be at low ranks (16, 17, 18, and 22th) which implies that they have less weights or have no effect toward lesion classification. Thus, energies were excluded from the feature list, leaving only 19 features, and this list then fed to reconstruct a new classifier. The test accuracy results of every fold are shown in Table 4. The average cross validation accuracy of 19 features is approximately improved by 2%, compared to 23 features.

Table 4 Test accuracy of every fold of 19 features

i^{th} Fold										Average
1	2	3	4	5	6	7	8	9	10	
50	77.78	60	77.78	60	77.78	90	60	77.78	50	68.11

The best model using 19 features is at 7th fold which achieved 100%, 90%, 99% of training, test, and overall accuracy as presented in Figure 31(a-c), respectively.

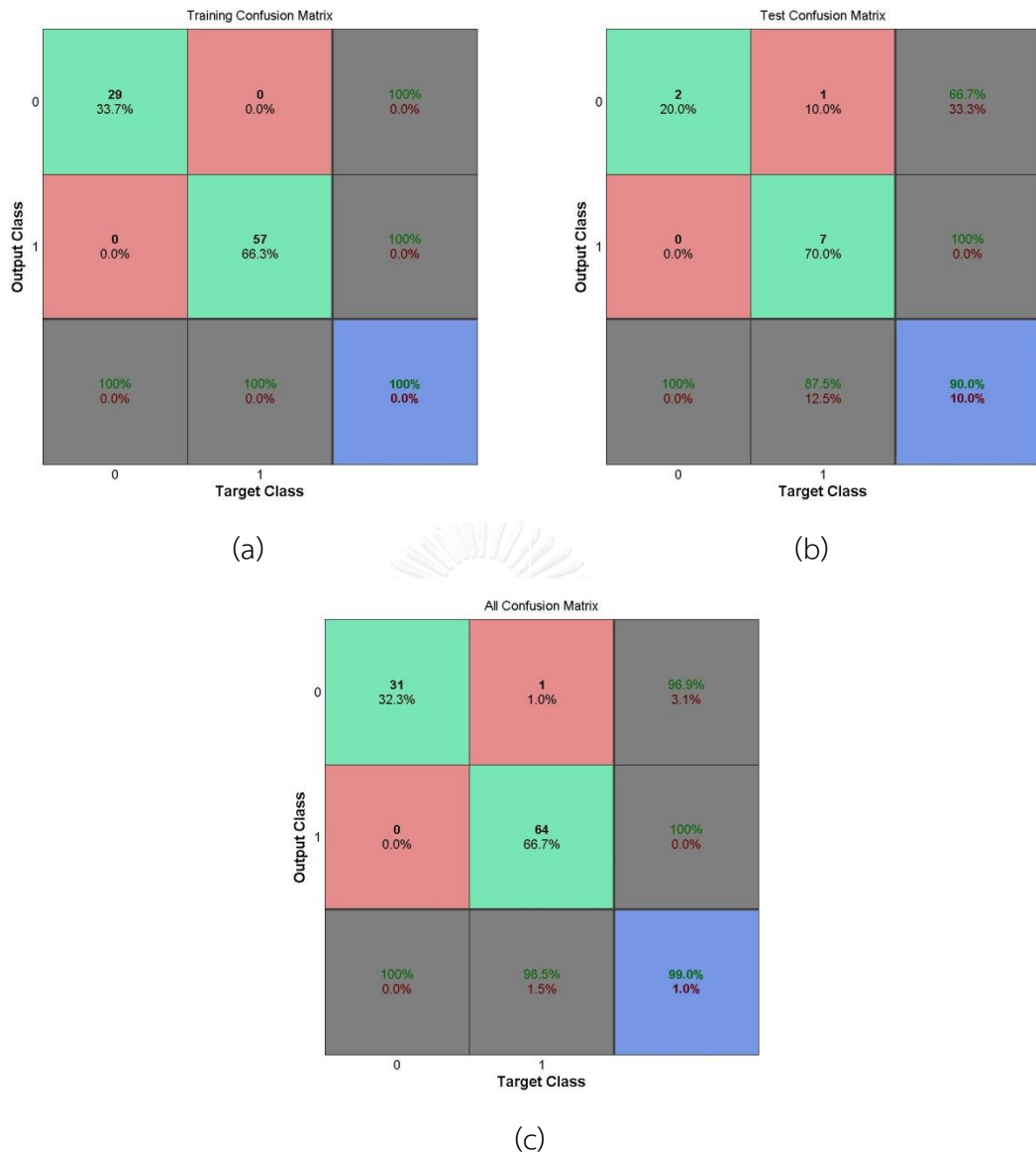


Figure 31 Confusion matrices of the best model of 19 features with (a) training (b) test (c) all data

Weights of 19 features of the best model are listed in Table 5. Our proposed features such as number of boundary sectors before interpolation, ray tracing and crossing count at 135-degree, 0-degree, number of longest consecutive boundary sectors before interpolation, ray tracing and crossing count at 45-degree and 180-degree might possibly be the key features to distinguish between benign and malignant lesion since they acquire the rank of 1-5 and 7, respectively.

Table 5 Weight rank of 19 features

No.	Feature Title	Rank
22	Boundary Sectors before Interpolation	1
21	Ray Count at 135-degree	2
18	Ray Count at 0-degree	3
23	Longest Consecutive Boundary Sectors	4
20	Ray Count at 45-degree	5
1	Entropy	6
19	Ray Count at 180-degree	7
17	Homogeneity at 135-degree	8
14	Homogeneity at 0-degree	9
16	Homogeneity at 45-degree	10
15	Homogeneity at 180-degree	11
2	Contrast at 0-degree	12
9	Correlation at 135-degree	13
8	Correlation at 45-degree	14
7	Correlation at 180-degree	15
6	Correlation at 0-degree	16
5	Contrast at 135-degree	17
3	Contrast at 180-degree	18
4	Contrast at 45-degree	19

The one and only incorrect classified sample in this model is demonstrated in Figure 32 which show unclear lesion boundary and high noise disturbance, results in wrong boundary detection and incorrect classification.

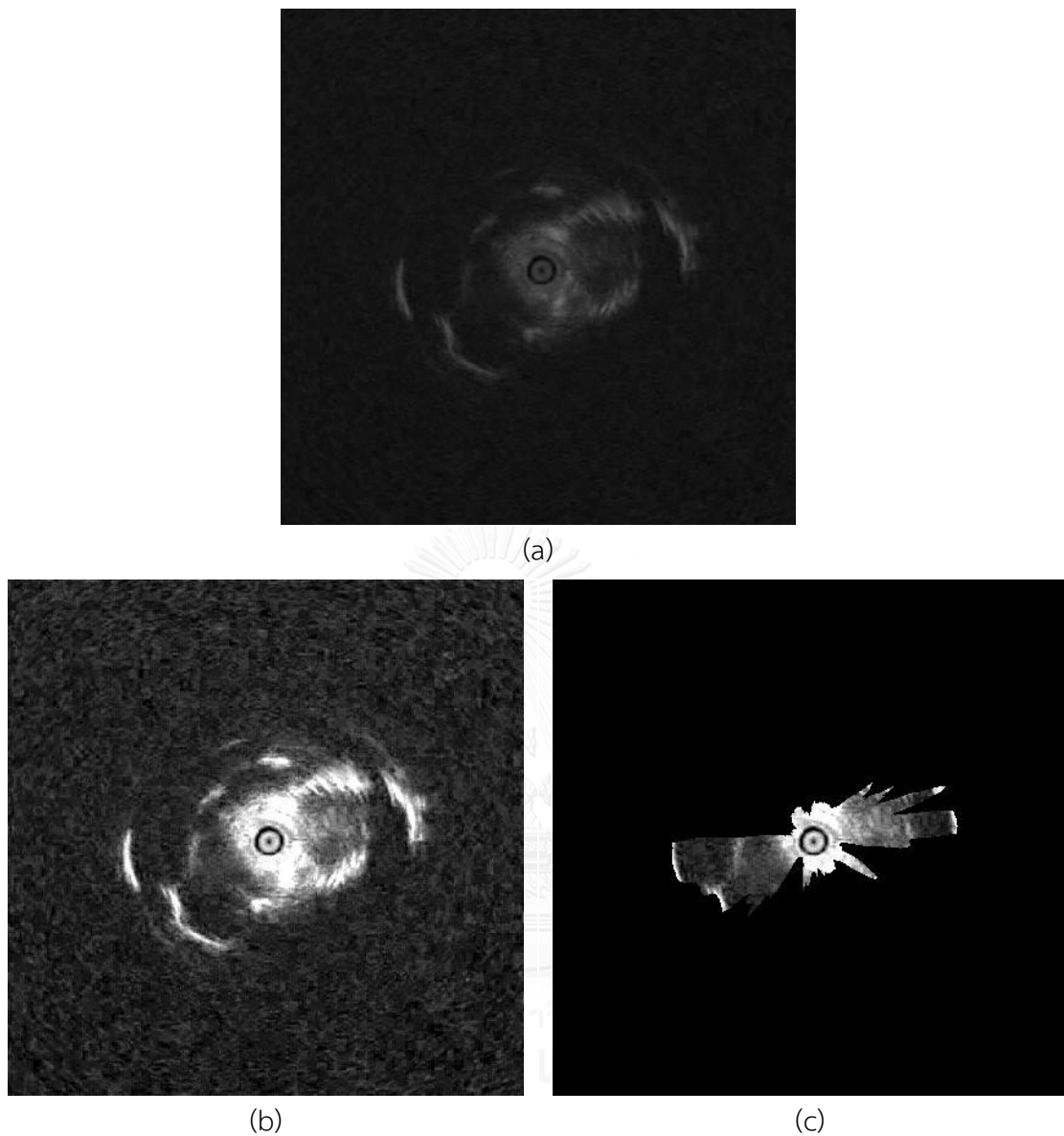


Figure 32 Sample of incorrect classification

(a) best frame (b) normalized best frame (c) normalized best frame overlaid by detected boundary

As a result, the proposed method of 19 features achieves the average cross validation test accuracy at 68.11% which is acceptable due to a novel research in the area; however, it may not be applicable and adequately reliable to practically apply in the real world without the doctor. Hence, there are some limitations that could be overcome to further improve this study which are described as follows:

First, one of the limitations that commonly known is the number of samples, which in this case, is composed of 96 lesions but might not be sufficient for generating accurate classification. The more input provides, the more solid result can be achieved. Thus, more data may be required to be collected and retested on this methodology to ensure the results.

For a traditional process, best frame was chosen manually by the doctor during the time of bronchoscopy or after which may require a lot of efforts for the doctors to review the video. As we select the best frame from our automatic approach, there may be some mistake. Hence, an evaluation of best frame selection should be separately performed prior to classification process. Besides proportion of lesion area and number of captured boundary sectors, intensity such as contrast or other conditions may be included in the best frame selection criteria to possibly increase the accuracy.

Additionally, as mentioned before that noise disturbance could affect boundary detection and classification. Noise reduction before boundary detection or feature calculation may be able to yield correct boundary detection and higher the accuracy.

In the step of boundary detection, there are some special cases of EBUS images which cause unexpected boundary detection, such as images with high presence of air linear bronchogram, as illustrated in Figure 33(a), and high absence of lesion margin as depicted in Figure 33(b). For the high presence of air bronchogram, the texture inside lesion is non-uniform and hyperechoic which is difficult to distinguish between boundary and air bronchogram, whereas, in high absence of lesion margin, more than 50% of lesion boundary disappear, due to an inappropriate frame selection. Thus, further study may be required to solve these problems.

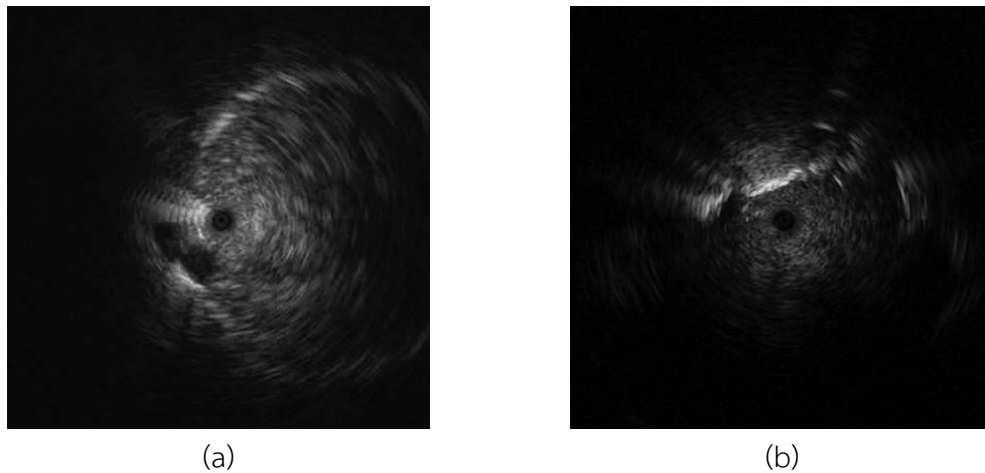


Figure 33 Sample of EBUS images
with (a) high presence of air linear bronchogram
(b) high absence of lesion margin

Moreover, discovering more useful features, deploying some standard feature selection and adjusting classifier's parameters or even testing on different classifiers may generate the better accuracy. However, as far as we tried other classifiers with default parameters such as decision tree (J48), Naïve Bayes, and SVM, we have found that neural networks with 10 hidden layers reveals the best accuracy among others.

In summary, this paper proposes a promising approach with acceptable accuracy to eliminate non-texture images from video, detect lesion boundary from EBUS image, select the best representative frame among the whole video, extract useful features, and finally classify the lesion according to those features. As a result, the proposed method could help assist the doctors in automatically classifying pulmonary lesions.

REFERENCES

1. J, F., et al. *GLOBOCAN 2012 v1.0, Cancer Incidence and Mortality Worldwide: IARC CancerBase No. 11*. 2013; Available from: <http://globocan.iarc.fr>.
2. Aberle, D.R., et al., *Reduced lung-cancer mortality with low-dose computed tomographic screening*. N Engl J Med, 2011. **365**(5): p. 395-409.
3. Physicians, A.C.o.C., *What If I Have a Spot on My Lung? Do I Have Cancer?* , in *Patient Education Guide*2004, American Colledge of Chest Physicians: Northbrook, Illinois, United States.
4. Yang, M.C., et al., *Diagnostic value of endobronchial ultrasound-guided transbronchial lung biopsy in peripheral lung cancers*. J Formos Med Assoc, 2004. **103**(2): p. 124-9.
5. Herth, F.J., A. Ernst, and H.D. Becker, *Endobronchial ultrasound-guided transbronchial lung biopsy in solitary pulmonary nodules and peripheral lesions*. Eur Respir J, 2002. **20**(4): p. 972-4.
6. Lin, S.M., et al., *Diagnostic value of endobronchial ultrasonography for pulmonary tuberculosis*. J Thorac Cardiovasc Surg, 2009. **138**(1): p. 179-84.
7. Shirakawa, T., et al., *Usefulness of endobronchial ultrasonography for transbronchial lung biopsies of peripheral lung lesions*. Respiration, 2004. **71**(3): p. 260-8.
8. Kuo, C.H., et al., *Diagnosis of peripheral lung cancer with three echoic features via endobronchial ultrasound*. Chest, 2007. **132**(3): p. 922-9.
9. Kurimoto, N., et al., *Analysis of the internal structure of peripheral pulmonary lesions using endobronchial ultrasonography**. CHEST Journal, 2002. **122**(6): p. 1887-1894.
10. McNitt-Gray, M.F., et al., *The effects of co-occurrence matrix based texture parameters on the classification of solitary pulmonary nodules imaged on computed tomography*. Computerized Medical Imaging and Graphics, 1999. **23**(6): p. 339-348.

11. Garra, B.S., et al., *Improving the distinction between benign and malignant breast lesions: the value of sonographic texture analysis*. Ultrasonic Imaging, 1993. **15**(4): p. 267-285.
12. Furuya, K., et al., *New classification of small pulmonary nodules by margin characteristics on high-resolution CT*. Acta Radiologica, 1999. **40**(5): p. 496-504.
13. Reddy, P. and L. Baker, *The Solitary Lung Nodule: The Solitary Lung Nodule*.
14. Winer-Muram, H.T., *The Solitary Pulmonary Nodule 1*. Radiology, 2006. **239**(1): p. 34-49.
15. Kuo, C.H., et al., *Echoic features as predictors of diagnostic yield of endobronchial ultrasound-guided transbronchial lung biopsy in peripheral pulmonary lesions*. Ultrasound Med Biol, 2011. **37**(11): p. 1755-61.
16. Lee, H.-W., et al., *Breast tumor classification of ultrasound images using wavelet-based channel energy and ImageJ*. Selected Topics in Signal Processing, IEEE Journal of, 2009. **3**(1): p. 81-93.
17. Sheppard, M.A. and L. Shih. *Efficient image texture analysis and classification for prostate ultrasound diagnosis*. in *Computational Systems Bioinformatics Conference, 2005. Workshops and Poster Abstracts. IEEE*. 2005. IEEE.
18. Singh, M., S. Singh, and S. Gupta. *A new measure of echogenicity of ultrasound images for liver classification*. in *Electrical and Computer Engineering (CCECE), 2011 24th Canadian Conference on*. 2011. IEEE.
19. Lloyd, S., *Least squares quantization in PCM*. Information Theory, IEEE Transactions on, 1982. **28**(2): p. 129-137.
20. Ester, M., et al. *A density-based algorithm for discovering clusters in large spatial databases with noise*. in *Kdd*. 1996.
21. Chapra, S.C., *Applied numerical methods*. McGraw Hill, New York, 2012.
22. Gonzalez, R.C., R.E. Woods, and S.L. Eddins, *Digital image processing using MATLAB*. Upper Saddle River, NJ: Prentice Hall, 2004.
23. Whitted, T. *An improved illumination model for shaded display*. in *ACM SIGGRAPH 2005 Courses*. 2005. ACM.

24. Marr, D., *Vision: A computational investigation into the human representation and processing of visual information*, Henry Holt and Co. Inc., New York, NY, 1982: p. 2-46.
25. Egmont-Petersen, M., D. de Ridder, and H. Handels, *Image processing with neural networks—a review*. *Pattern recognition*, 2002. **35**(10): p. 2279-2301.
26. Stehman, S.V., *Selecting and interpreting measures of thematic classification accuracy*. *Remote sensing of Environment*, 1997. **62**(1): p. 77-89.

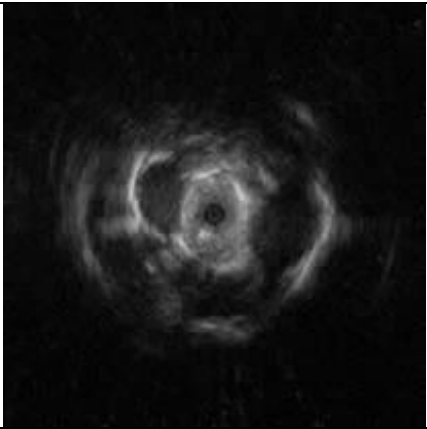
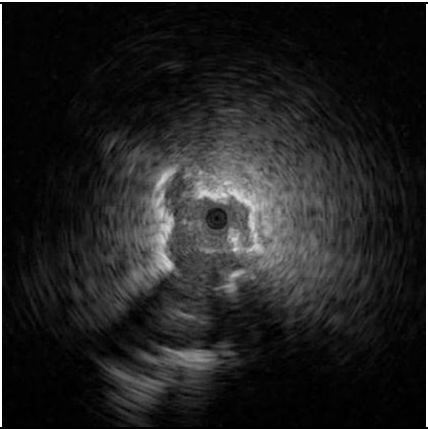
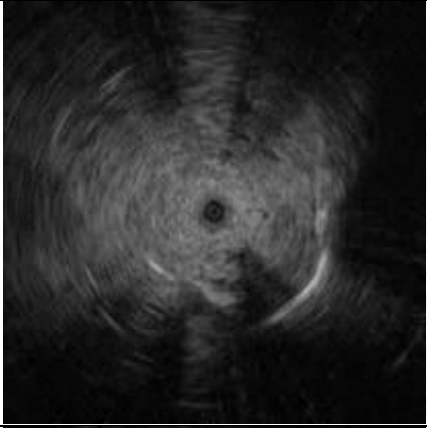
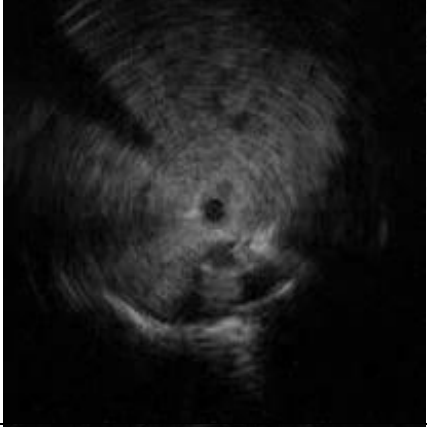
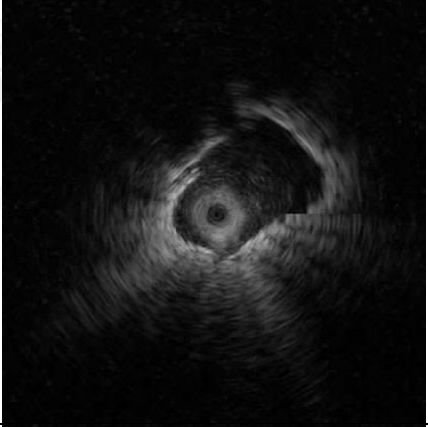
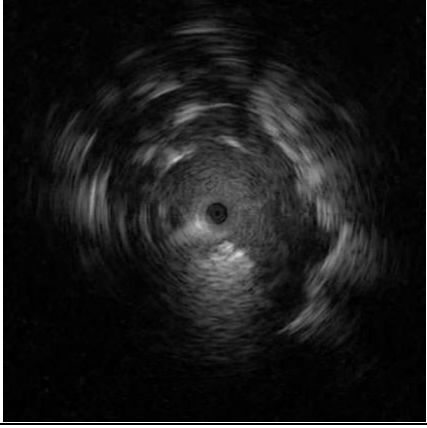
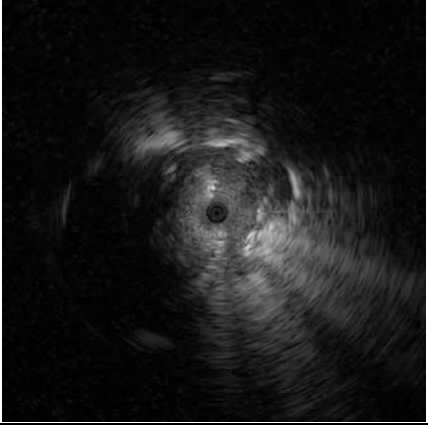


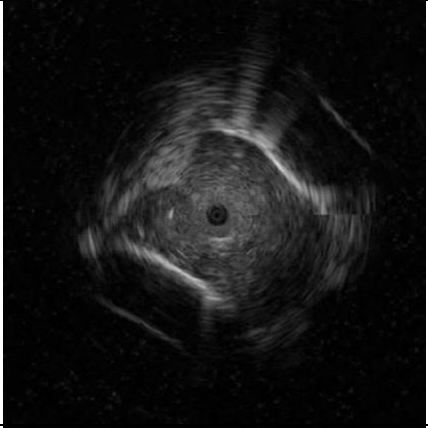
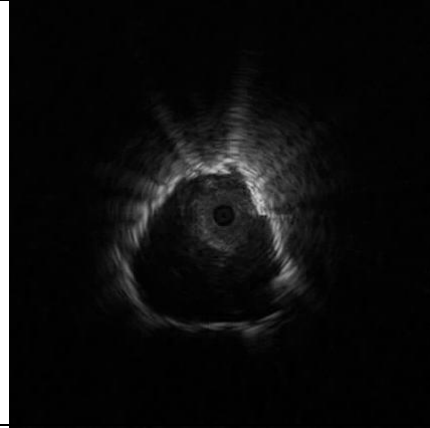
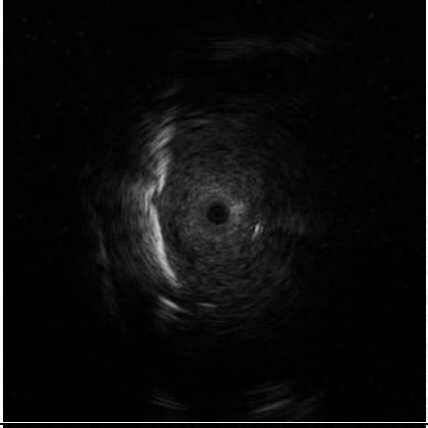
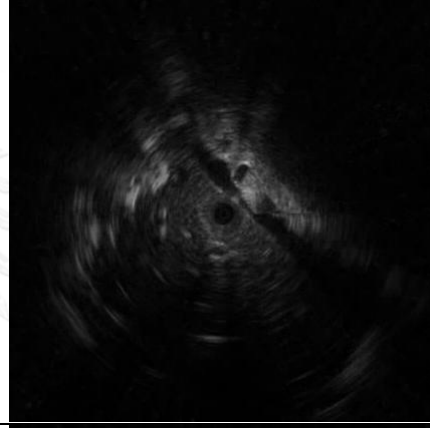
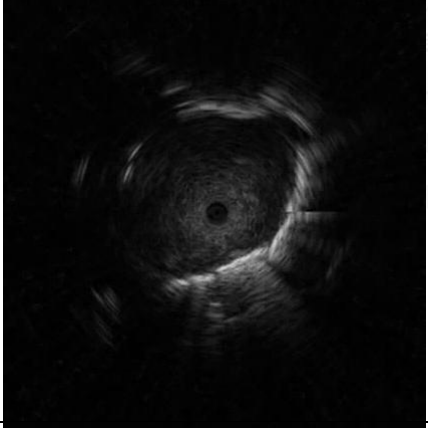
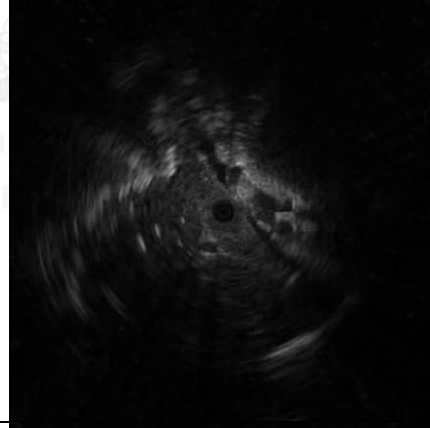
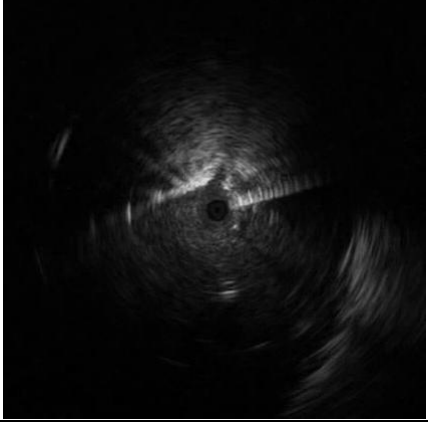
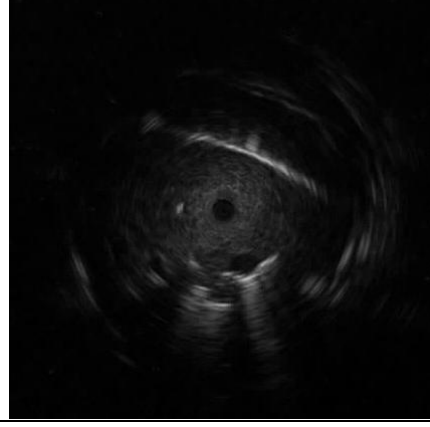


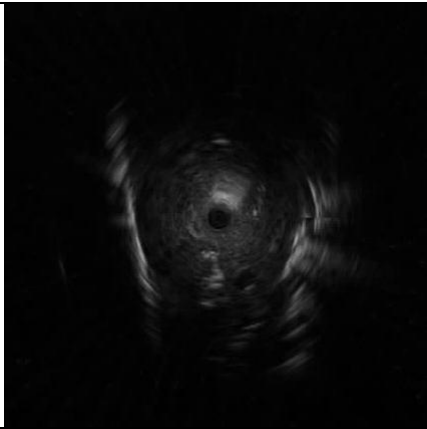
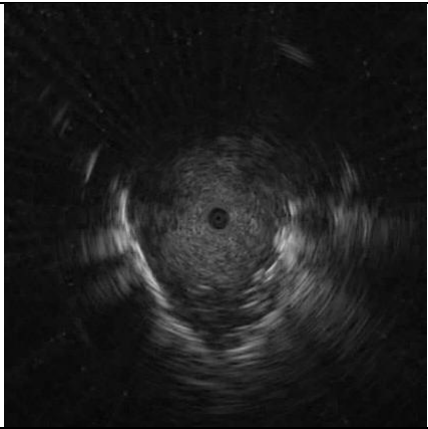
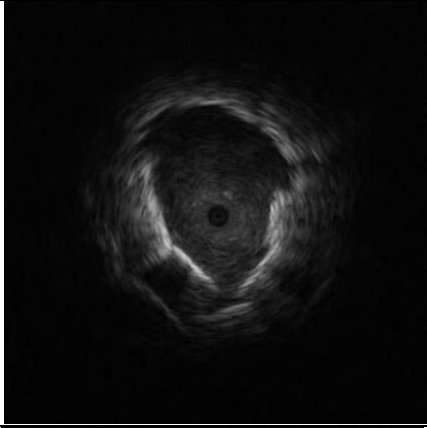
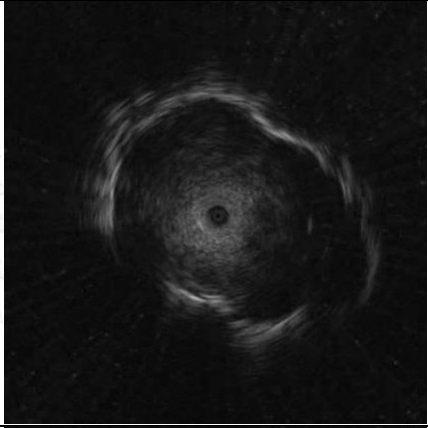
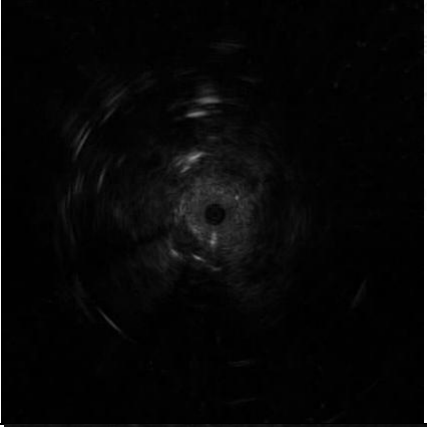
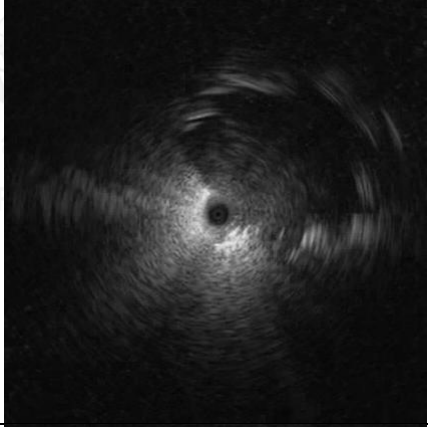
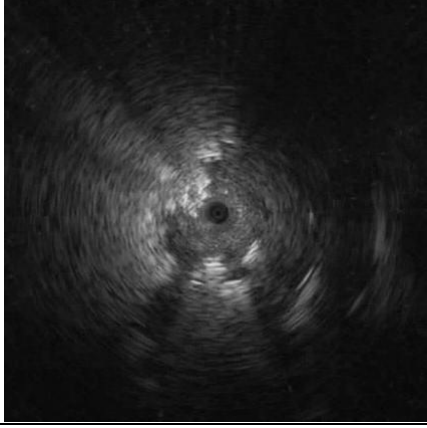
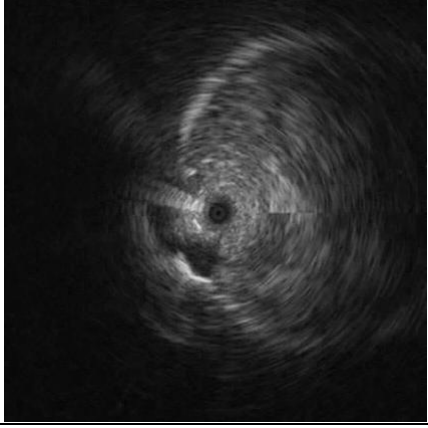
APPENDIX

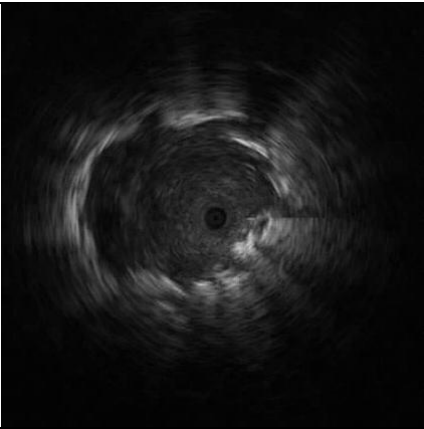
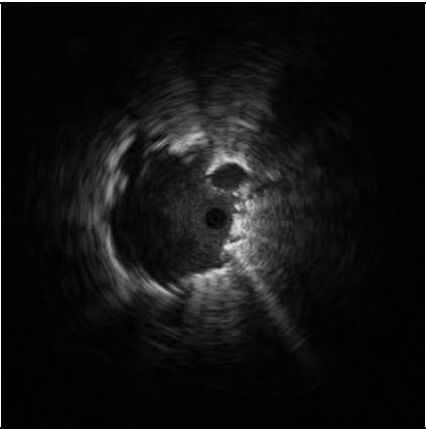
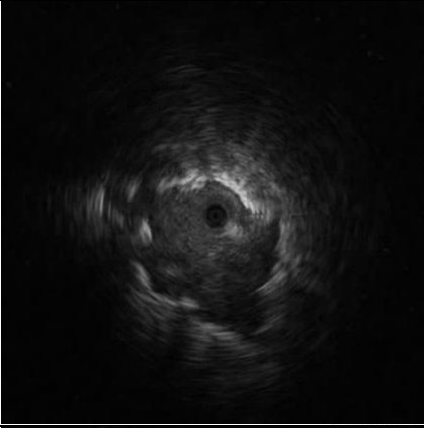
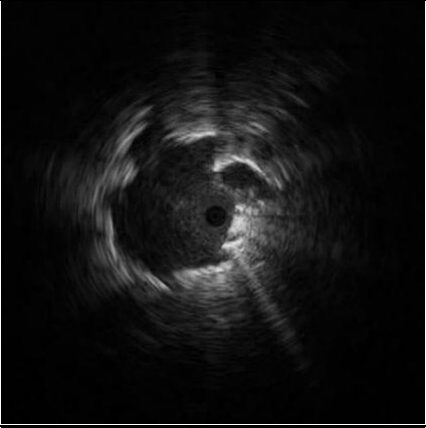
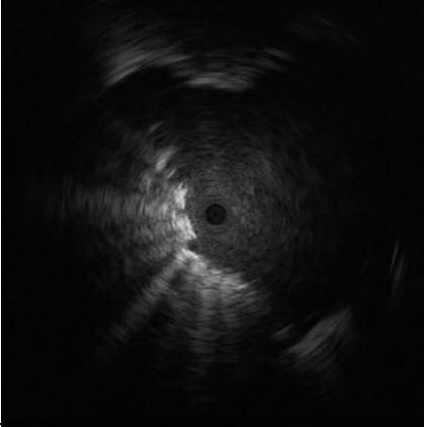
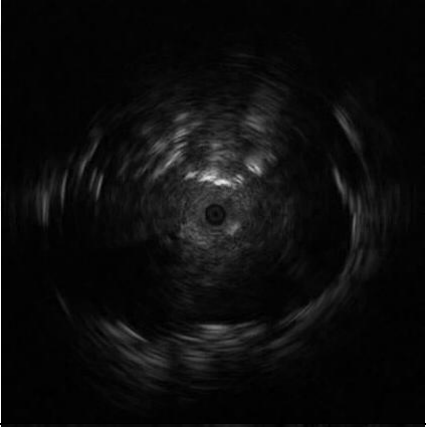
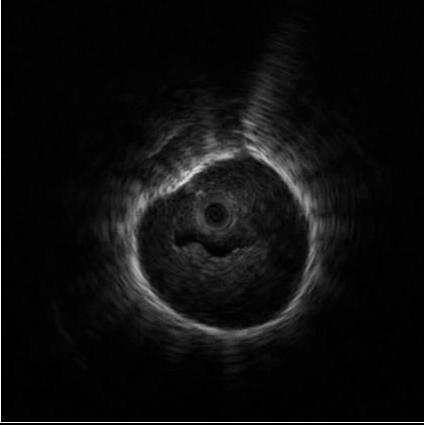
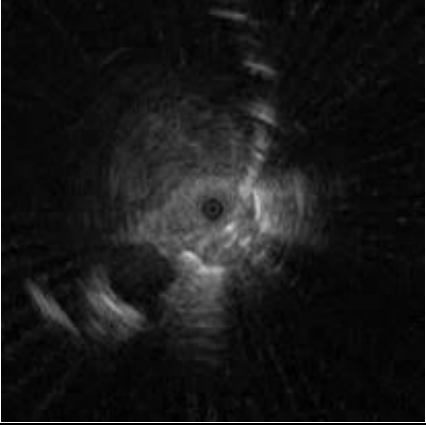
จุฬาลงกรณ์มหาวิทยาลัย
CHULALONGKORN UNIVERSITY

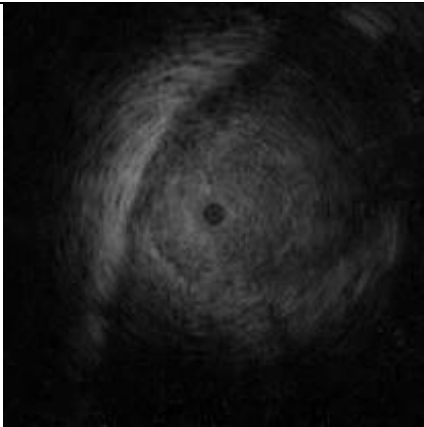
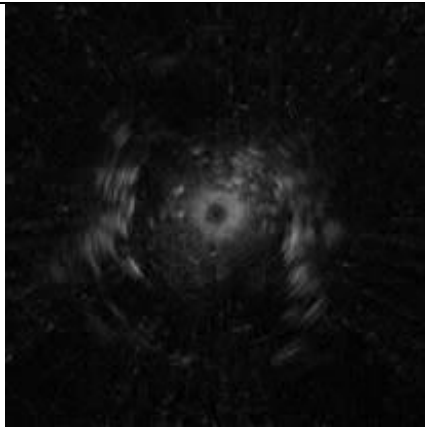
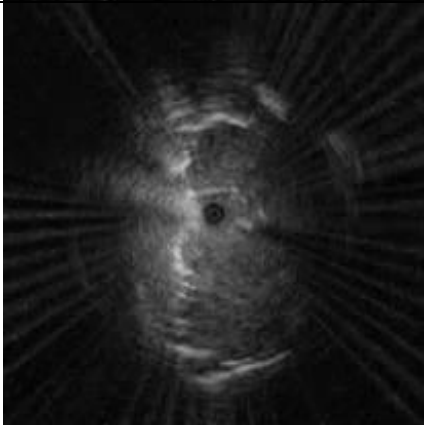
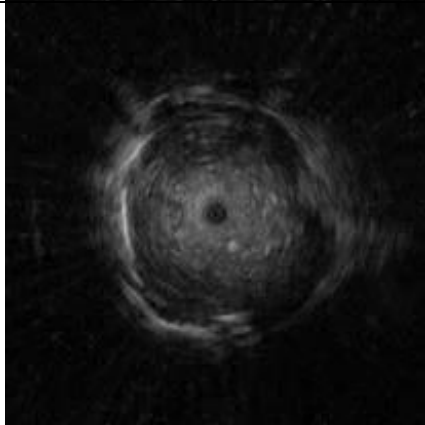
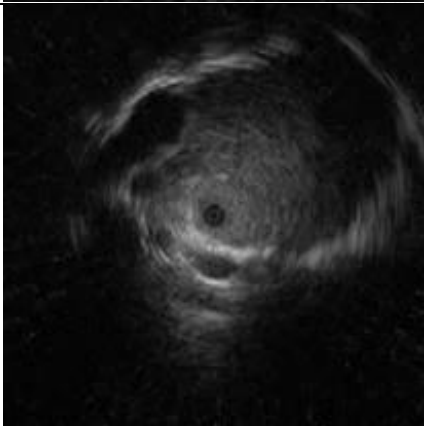
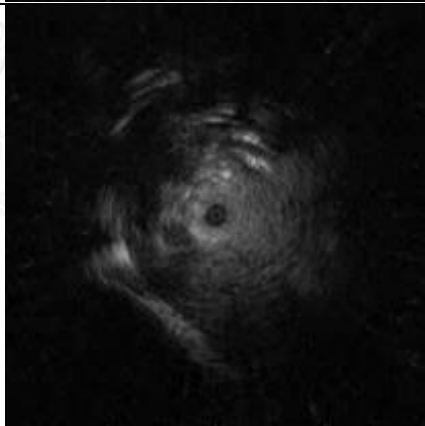
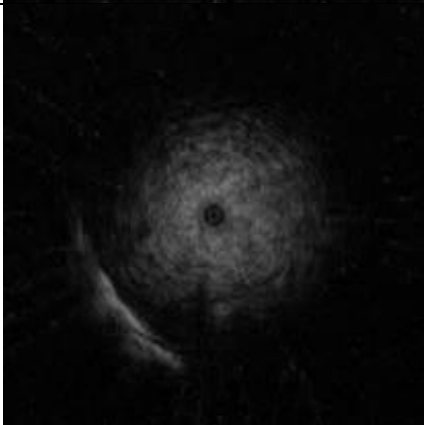
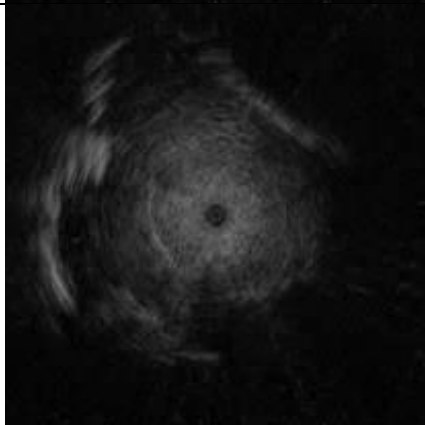


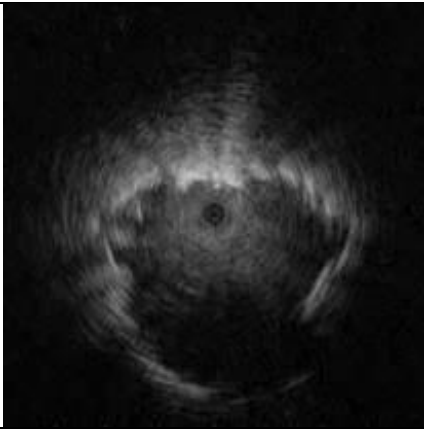
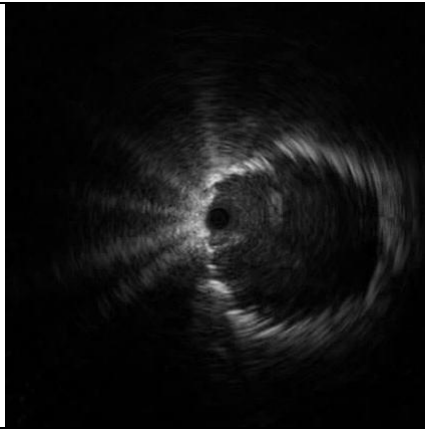
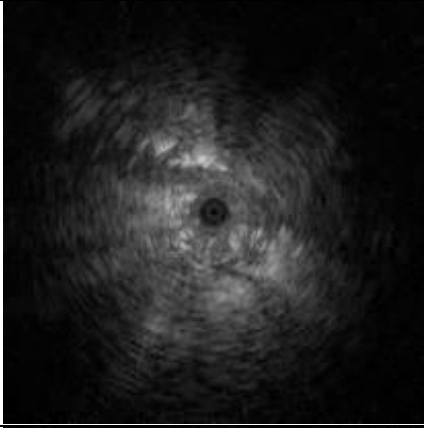
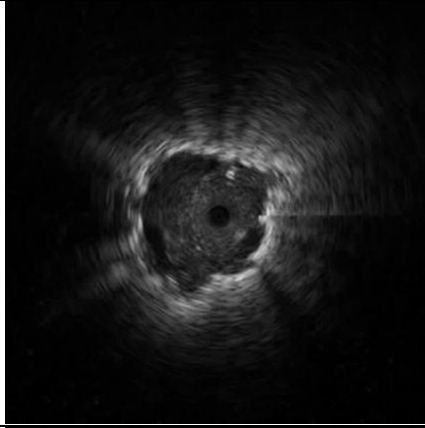
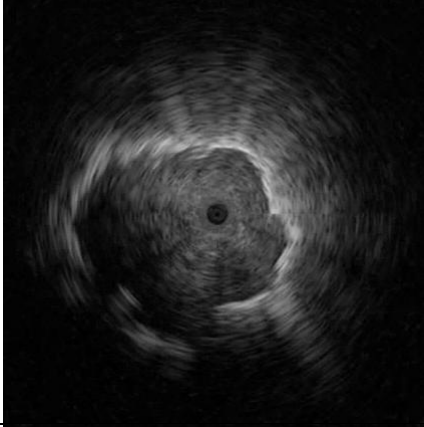
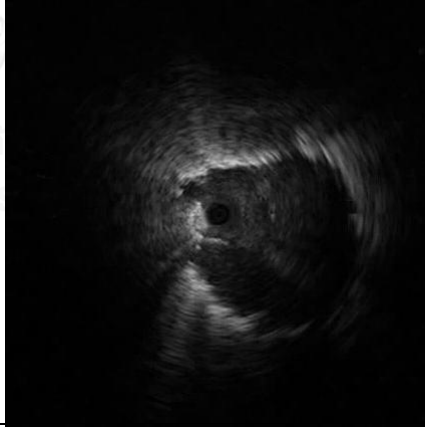
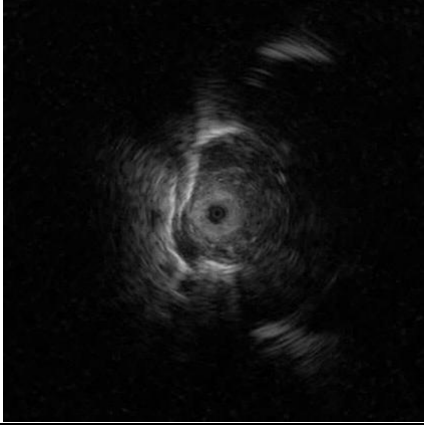
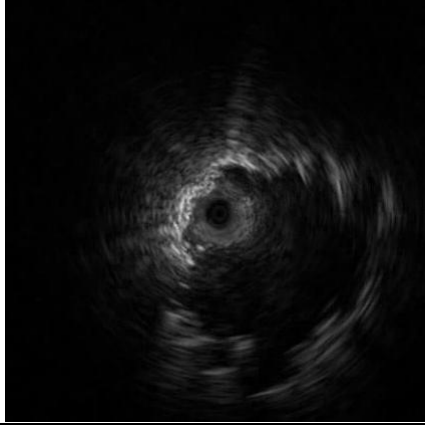
File	Best Frame	File	Best Frame
17		37	
23		38	
24		42	
6		44	

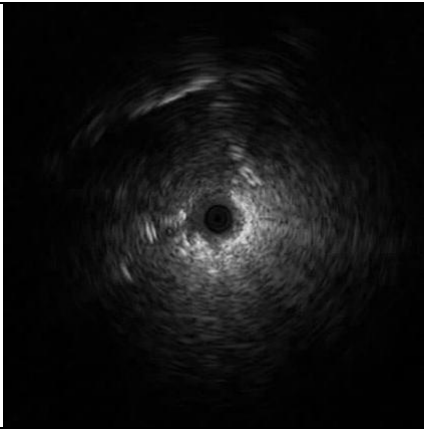
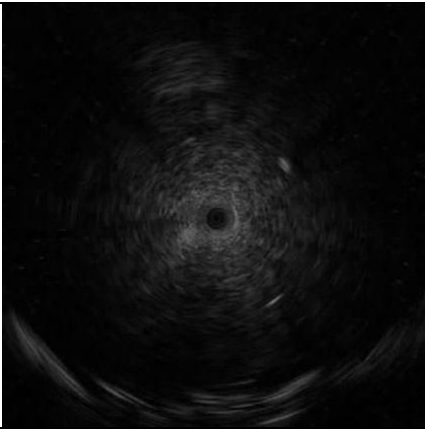
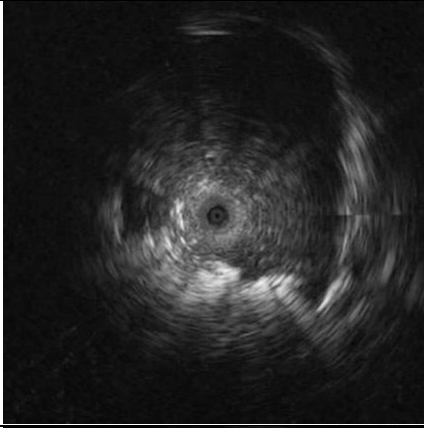
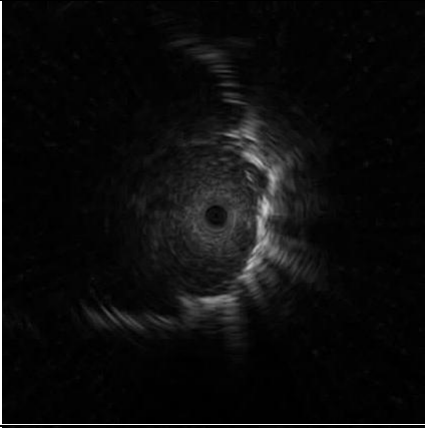
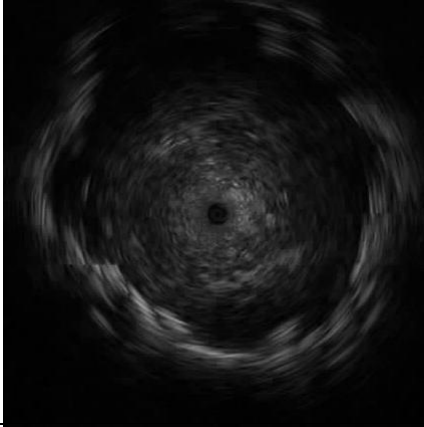
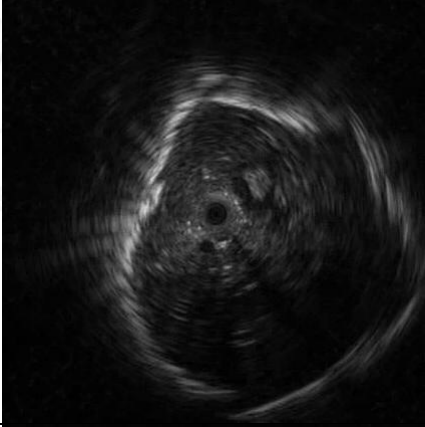
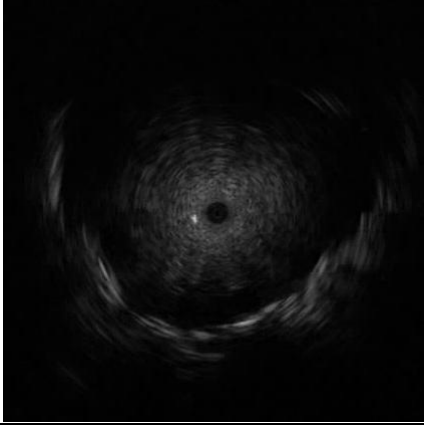
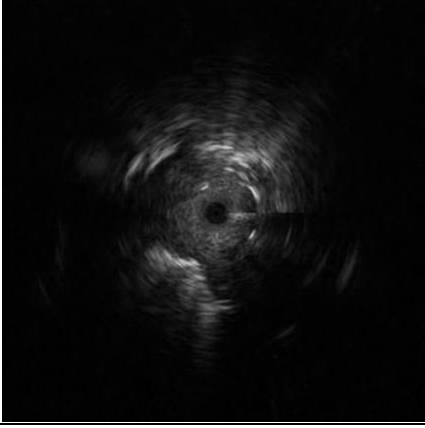
File	Best Frame	File	Best Frame
52		94	
59		97	
70		98	
74		104	

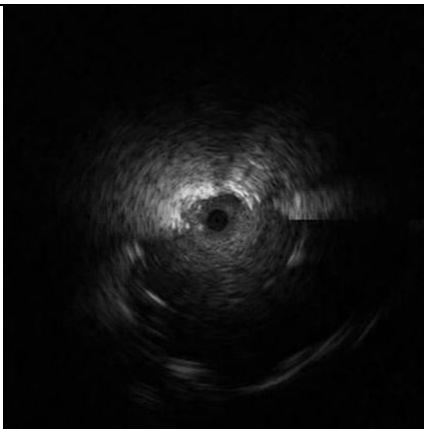
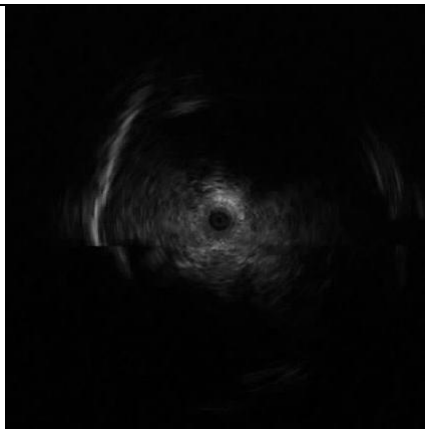
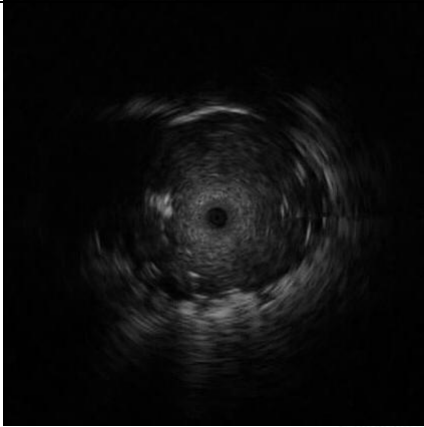
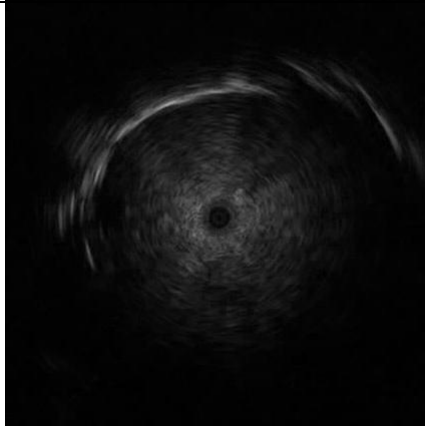
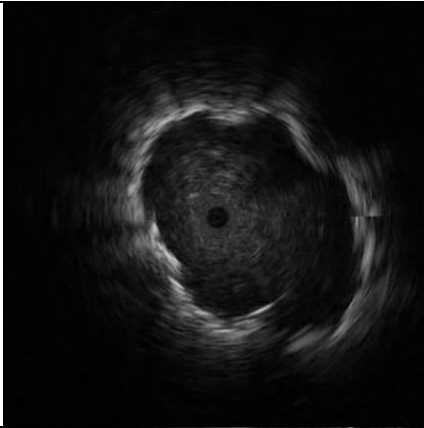
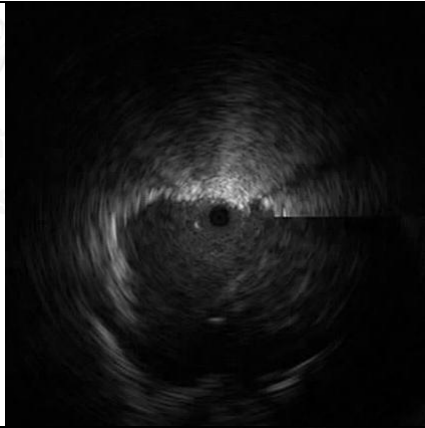
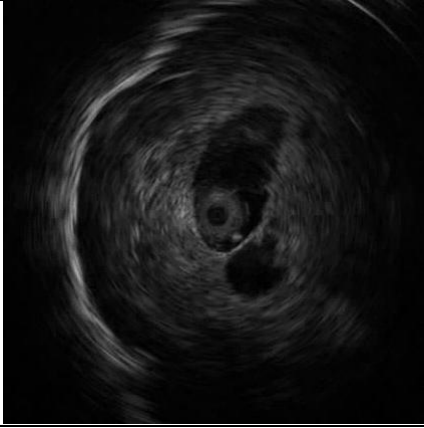
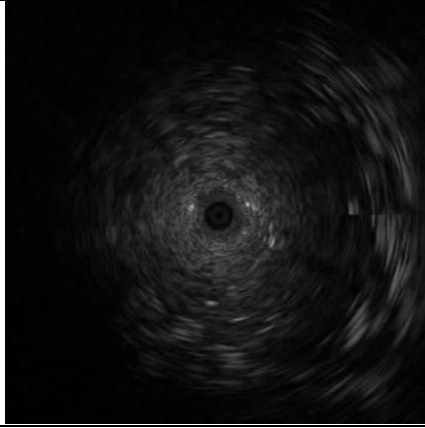
File	Best Frame	File	Best Frame
105		123	
112		124	
114		127	
121		134	

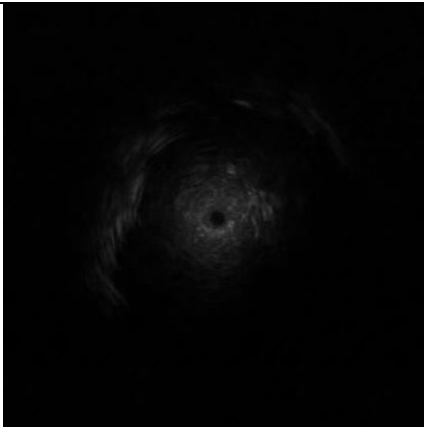
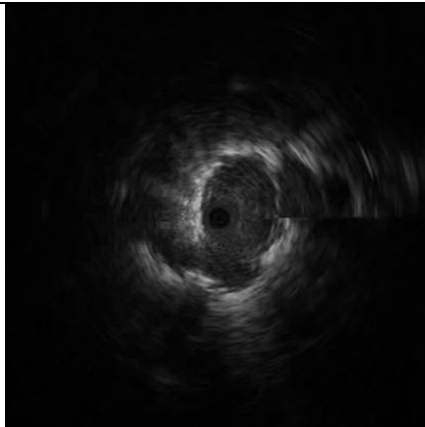
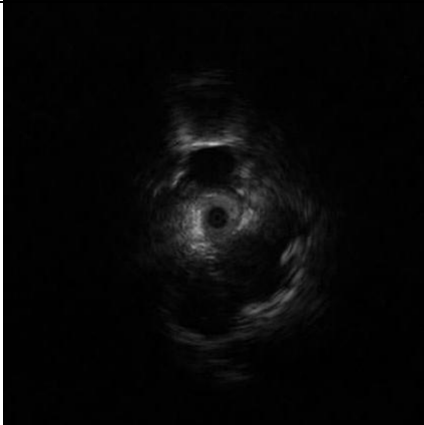
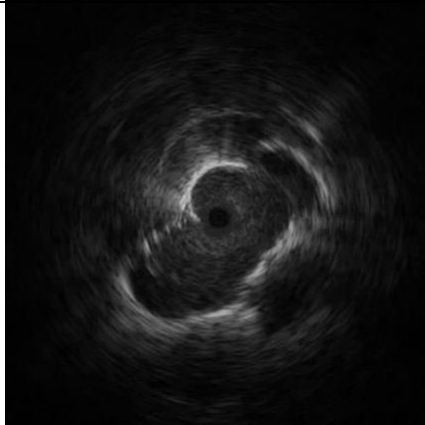
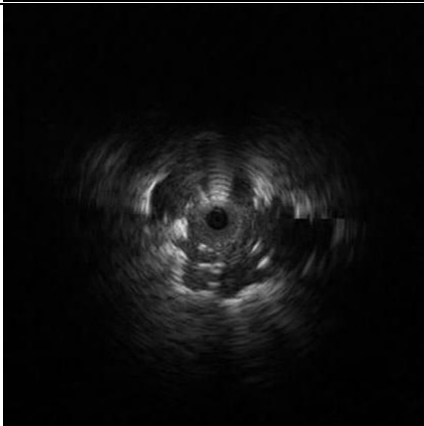
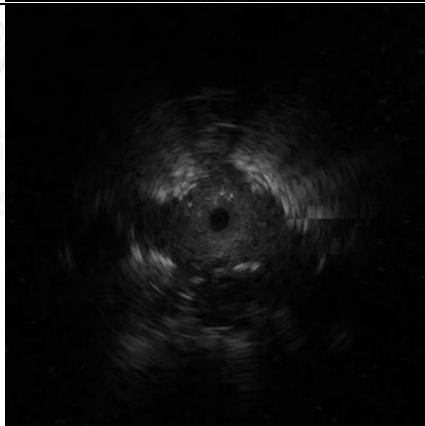
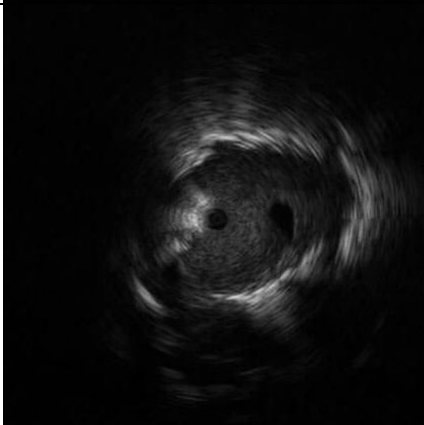
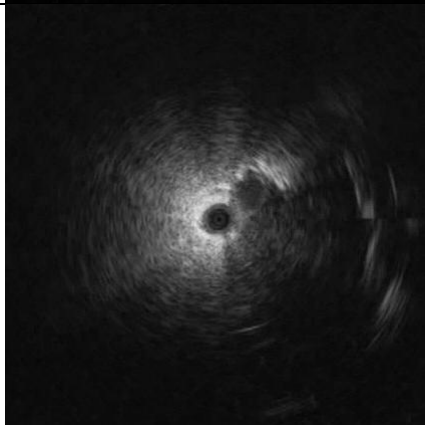
File	Best Frame	File	Best Frame
161		186	
162		187	
173		199	
184		3	

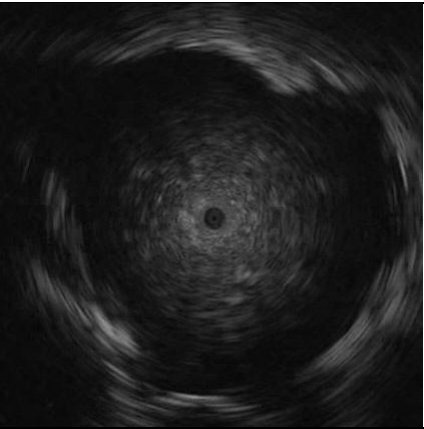
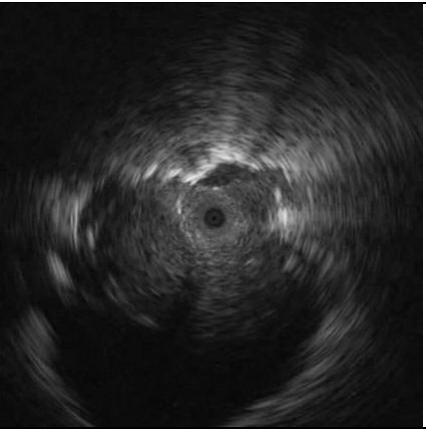
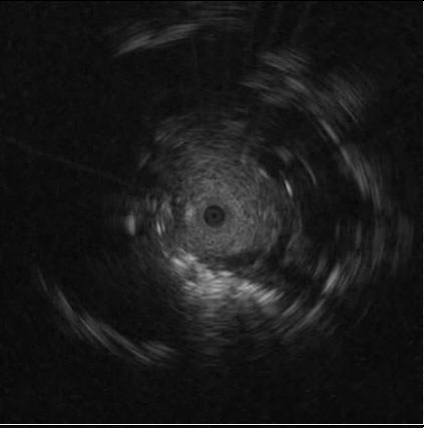
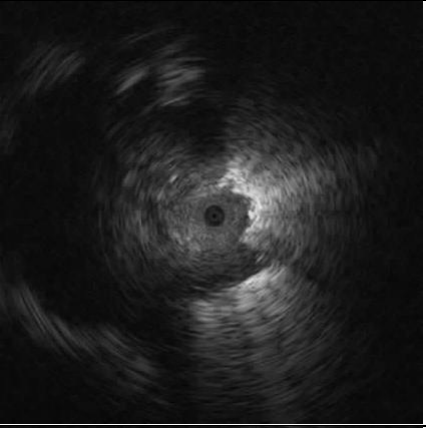
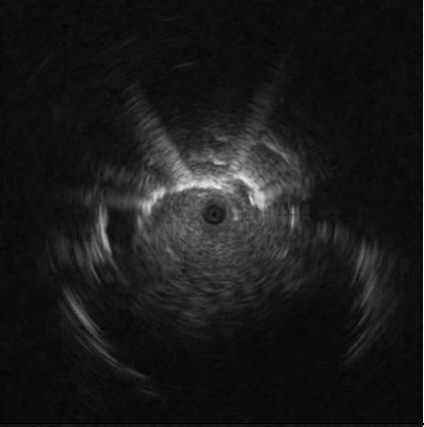
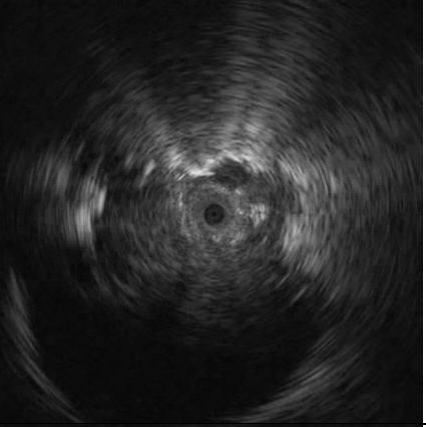
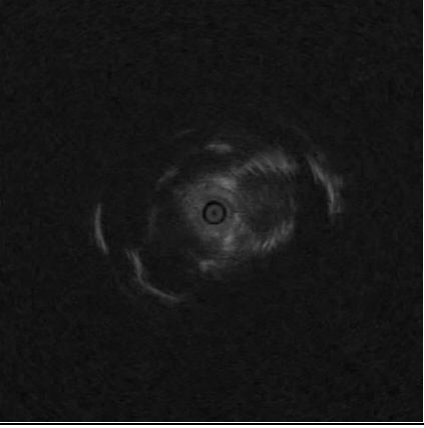
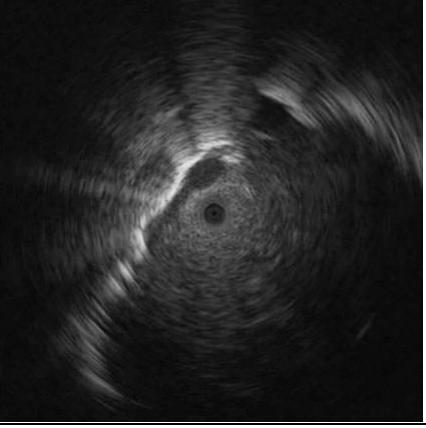
File	Best Frame	File	Best Frame
4		11	
5		12	
8		19	
10		20	

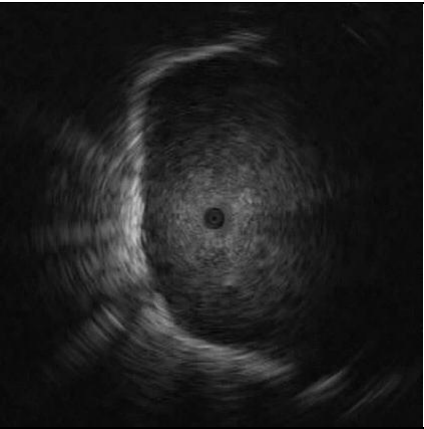
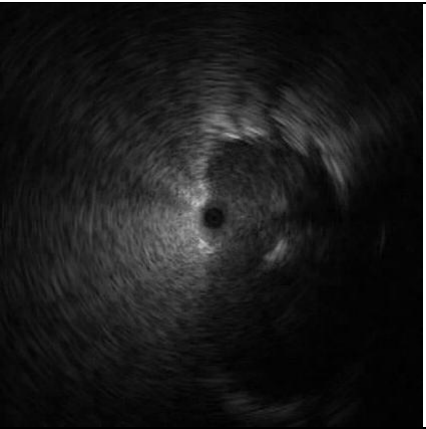
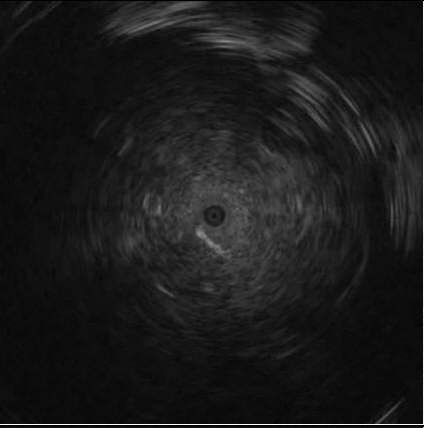
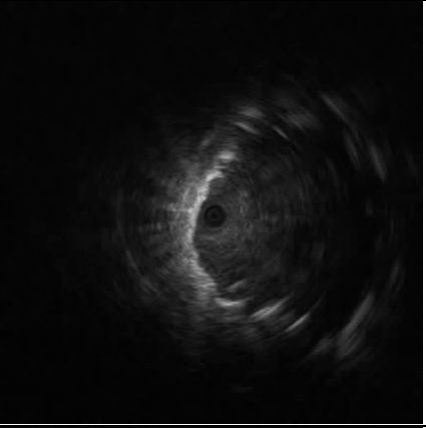
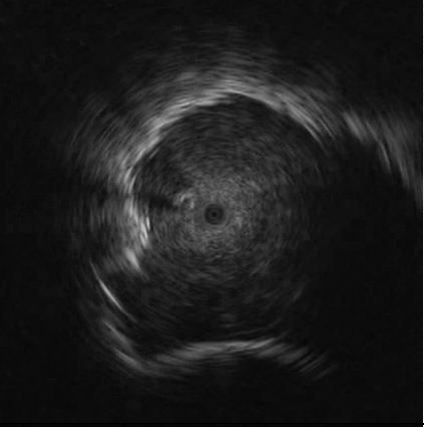
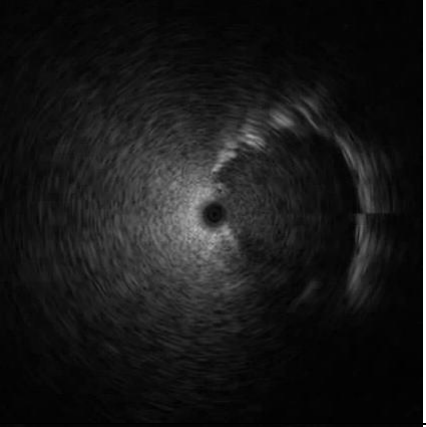
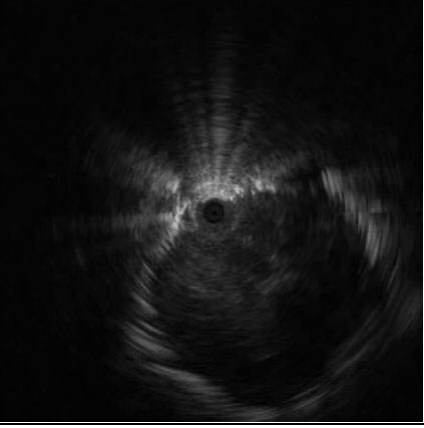
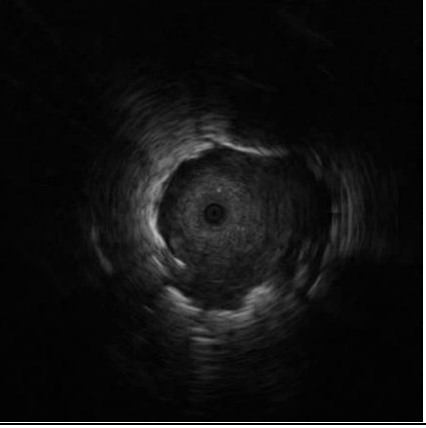
File	Best Frame	File	Best Frame
21		53	
33		54	
39		55	
45		57	

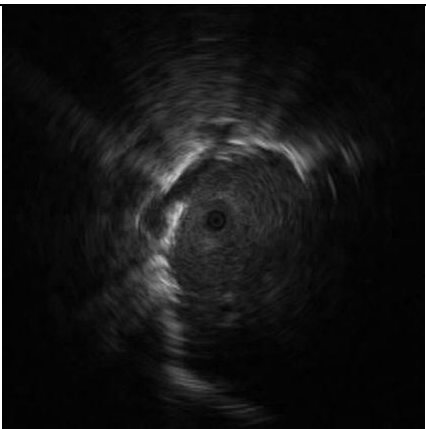
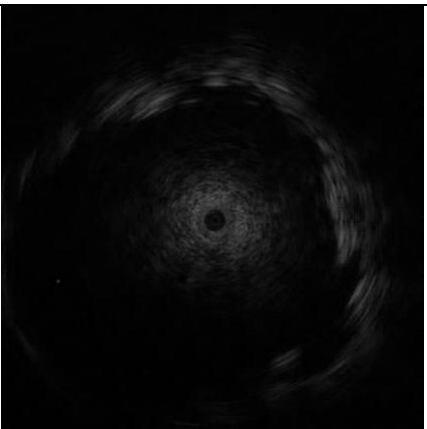
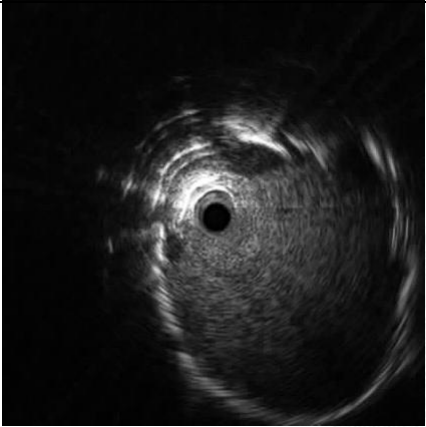
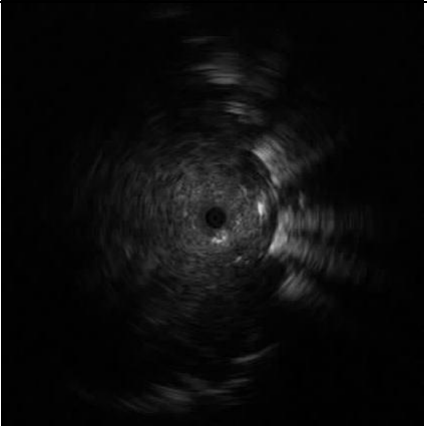
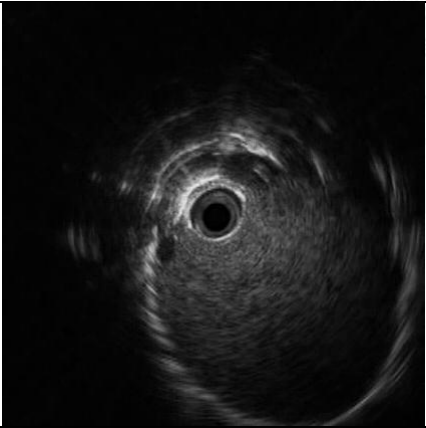
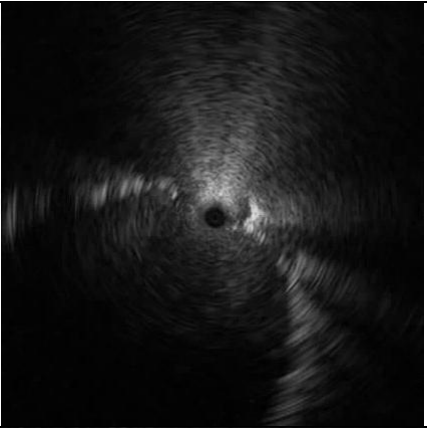
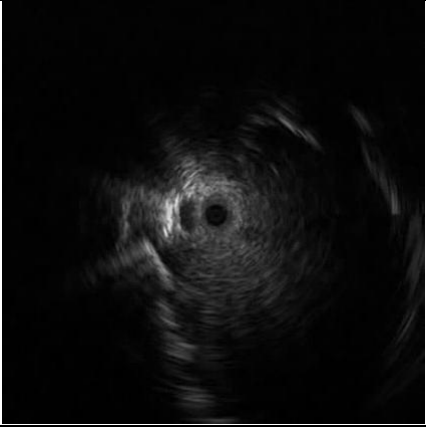
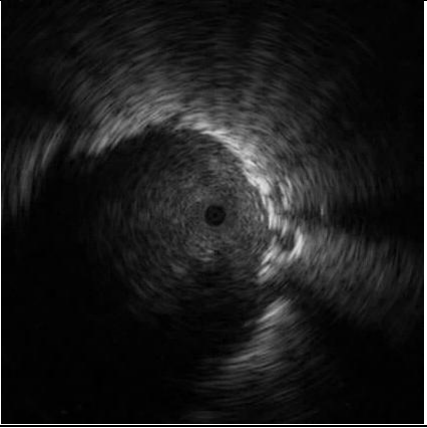
File	Best Frame	File	Best Frame
58		63	
60		68	
61		71	
62		75	

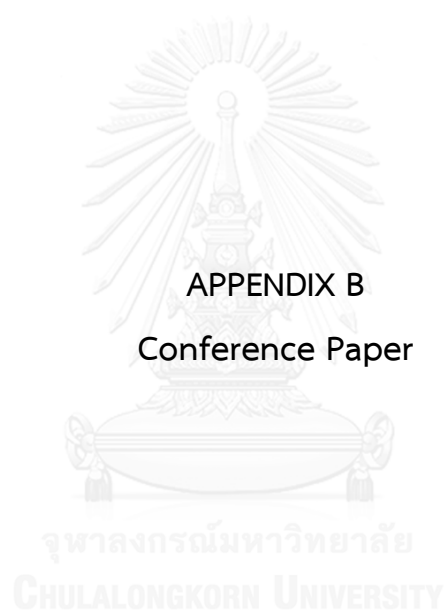
File	Best Frame	File	Best Frame
76		80	
77		81	
78		87	
79		89	

File	Best Frame	File	Best Frame
90		106	
91		107	
92		113	
93		120	

File	Best Frame	File	Best Frame
125		139	
129		140	
135		141	
138		143	

File	Best Frame	File	Best Frame
144		158	
147		163	
154		167	
157		170	

File	Best Frame	File	Best Frame
177		185	
180		189	
181		197	
183		198	



Pulmonary Lesion Boundary Detection from an Endobronchial Ultrasonogram using Polar Sector Maximum Intensity

Wannapon Suraworachet¹, Rajalida Lipikorn¹
& Anan Wattanatham, MD²

¹Machine Intelligence and Multimedia Information Technology (MIMIT) Laboratory, Department of Mathematics and Computer Science, Faculty of Science, Chulalongkorn University, Bangkok, Thailand.

²Pulmonary and Critical Care Division, Department of Medicine, Phramongkutklo Hospital, Bangkok, Thailand.

Abstract

This paper presents a method to detect pulmonary boundary from an endobronchial ultrasonogram which can automatically assist bronchoscopists to define the region of interests within obtained endobronchial ultrasonograms images in order to perform further texture analysis aiming to diagnose the lesion. Multiple image processing techniques are performed to capture lesion boundary, starting from transforming image pixels from Cartesian coordinates into Polar coordinates, iterating over each degree to find pixels with the highest intensity, grouping candidate pixels with Density-Based Spatial Clustering of Applications with Noise (DBSCAN), eliminating isolate groups by second order derivatives, smoothing an image using moving average filtering, connecting remaining pixels to form a boundary using cubic spline interpolation. The total of 200 images, which composed of 100 benign and 100 malignant images, are used to evaluate the proposed method. As a result, the correlation between the obtained boundary and the ground-truth data is 93.92%.

Keywords: boundary detection, endobronchial ultrasound, DBSCAN, moving average filter, cubic spline interpolation, polar sector.

1. Introduction

Lung cancer is known as the major cause of death worldwide due to its high mortality rate [1]. The prompt screening of risky patients can help decrease the rate of mortality down by 80% [2] because small tumors are mostly identified as an infection or scar tissues, but not as cancer [3].

In order to diagnose pulmonary nodules, bronchoscopy with transbronchial lung biopsy (TBLB) is recommended due to its efficiency, especially when guided by endobronchial ultrasound (EBUS). EBUS is inserted via bronchoscope to actively visualize internal textures of lesions, which can provide the diagnosis

yield of 60-80% [4-6], higher than conventional CT localization [5] or fluoroscopy, which can expose patients to harmful radiation [4,7].

Apart from the benefits of EBUS visualization, the characteristics of EBUS image also have a correlation with the histopathology of the lesions. According to Kurimoto and colleagues, their study reveals that 92% of lesions with homogeneous pattern are benign, whereas 99% of lesions with heterogeneous pattern are malignant [8]. In addition, the results from another research show that the presence of at least two out of three features of echoic patterns in EBUS image including heterogeneous pattern, continuous margin and the absence of a linear-discrete air bronchogram represents the malignancy of the lesions [9]. All these findings can possibly be a breakthrough to innovate a computer-aided diagnosis system and thus, lower the amount of biopsy and the pathology examination time for diagnosing further pulmonary lesions.

According to [10], an average examination time for bronchoscopy is 26.6 minutes, which results in 39,900 possible images due to video frame rate of 25-frame per second. Selection of the best frame or image for representing lesion features is significant for diagnostic and further process. Since the best representative frame is considered to have the largest lesion region among others, boundary detection is thus essential in order to calculate the lesion area to select a representative frame.

Moreover, boundary detection is useful for identifying continuous or non-continuous margin, which is one of the key features to classify benign and malignant lesions. Additionally, other crucial features including homogeneous or heterogeneous pattern and absence or presence of air bronchogram are required to firstly identify region of interests before measurement.

Various algorithms for detecting boundary have been proposed for ultrasound images used in different organs and tissues of human body, especially, in breast and prostate. However, there is no recent study on detecting lesion boundary from EBUS. Since EBUS image is captured within a lesion using mechanical radial ultrasound miniature probes, the perspective of lesion is not similar to other types of ultrasound images which are mostly coronal views deriving from curvilinear ultrasound probes. Therefore, in order to make use of these distinct EBUS image characteristics, a novel algorithm to detect the boundary of pulmonary lesion of an EBUS image with optimum accuracy is proposed in this paper to further adapt an efficient pulmonary lesion classification system.

For clarity of presentation, this paper is divided into 4 sections. Section 2 and 3 describe proposed methodology and experimental results, respectively. Finally, section 4 presents discussion and conclusions.

2. Proposed Methodology

2.1 Preprocessing

Sample images that were captured randomly from endobronchial ultrasound video, are converted to gray scale. After that, each image is cropped to eliminate

irrelevant components such as metadata written on the screen, leaving only an actual image to be processed as shown in Fig. 1.

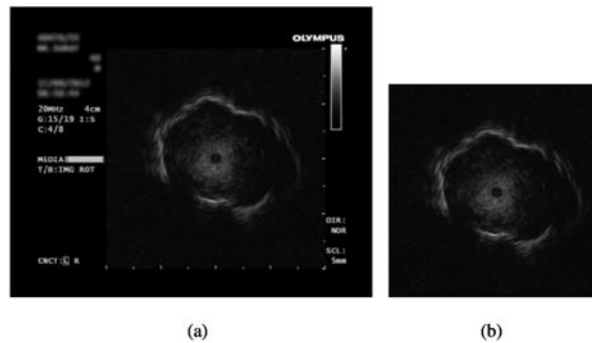


Fig. 1: Image (a) before and (b) after preprocessing

2.2 Polar Sector Maximum Intensity

2.2.1 360-Degree Iterative Maximum Intensity Detection

Each pixel of an image is transformed from Cartesian coordinates (x, y) into polar coordinates (radius, theta) by firstly assigning the central pixel of an image as the origin of the polar system. Then, an image is divided into 360 sectors according to the degree of theta. Regarding echogenicity of the boundary, the actual boundary tends to have hyperechoic characteristics. Thus, a pixel with maximum intensity of each sector is selected as a candidate pixel. If there are two or more pixels having the same maximum intensity, the innermost pixel or the pixel with the shortest radius is selected. After the candidate pixels of all sectors are obtained, the new origin of the polar system is calculated from these candidate pixels. Next, the process of finding a pixel with maximum intensity of each sector is iterated again until the new origin is stable or is the same as the previous origin. As a result, the final candidate pixels are illustrated in Fig. 2(a).

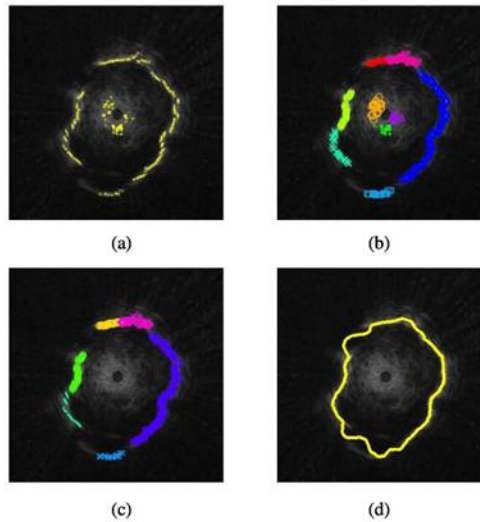


Fig. 2: (a) The result of 360-degree iterative maximum intensity detection
 (b) The result of DBSCAN iteration
 (c) The result of elimination by second order derivatives
 (d) The final result of proposed boundary detection

2.2.2 Density-Based Spatial Clustering of Applications with Noise (DBSCAN) iteration

After acquired all candidate pixels, these pixels have to be identified whether they are part of a lesion boundary or not by using Density-Based Spatial Clustering of Applications with Noise (DBSCAN), which was proposed by [11], as a clustering method to divide them into clusters. Assuming that the minimum number of points to form a cluster is 10; otherwise, they are considered as noise. Each cluster forms a boundary segment. By heuristic evaluation, 10 pixels are minor enough to separate coordinates into consecutive boundary segments, and major enough to consider a high density group of coordinates as another segment, but not to recognize them as noise. Then, statistical data of individual clusters, including standard deviation of segments' radius, are calculated. DBSCAN is iterated over a cluster that has a standard deviation of radius higher than 10. If all clusters have their standard deviation of radius lower than 10 or they are highly coherent which cannot be subdivided any further, this process terminates. Fig. 2(b) depicts a sample result of iteration over DBSCAN. Each cluster is labelled by different color and marker specifier.

2.2.3 Second Order Derivatives

In order to eliminate clusters that do not belong to a boundary, but are actually noise with high intensity, second order derivatives of local mean radius of each cluster is used and can be calculated according to eqn. (1). If there is any cluster, whose second order derivatives of local mean radius is higher than the mean radius among three considering consecutive clusters and also has the local mean intensity lower than the global mean intensity, it will be removed. The result after performing elimination by second order derivative is shown in Fig. 2(c).

$$f''(x) = f(x-1) + f(x+1) - 2(f(x)) \quad (1)$$

where $x = 1, 2, \dots, nth$ clusters,
 n is the number of clusters arranged by theta,
 $f(x)$ is the average radius of xth cluster ,
 $f(x-1)$ is the average radius of $(x-1)th$ cluster,
 $f(x+1)$ is the average radius of $(x+1)th$ cluster ,
 $f''(x)$ is the second order derivative of cluster xth .

2.2.4 Polar Coordinate System Reference Adjustment

After eliminating noise, the position in polar coordinate (radius, theta) of each remaining pixel is recalculated according to the new reference which is the center of an image, not the unstable center as in 2.2.1. In order to be consistent and to make a comparison across all data, the center of reference or the origin of polar system should be the same which is at the image center.

2.2.5 Smoothing by moving average filter

Next, the remaining pixels are smoothed using moving average filter [12] with a span of nine in order to filter out noise spikes and make the boundary to be less fluctuated, revealing only significant pixels of boundary.

2.2.6 Cubic Spline Interpolation

Finally, all of the pixels are reconnected to each other while the missing representative pixels are estimated by cubic spline interpolation with theta (x) and radius (y) as the input data. Consequently, a spline function is used to estimate the unknown radii to match with the given thetas in a specific range of -180 to 180 degree. The result of this process is demonstrated in Fig. 2(d).

3. Experimental Results

Input data are video files which are recorded during endobronchial ultrasonography and collected from Phramong Kutklao Hospital, Bangkok, Thailand. The data are composed of 10 samples of benign and 10 samples of malignant lesions. Additionally, the video file format is MPEG-1 with a dimension of 576 x 720 pixels or 288 x 352 pixels, and was captured at frame rate of 25 frames per second. Ten frames are randomly selected from each file.

Hence, there are 200 images in total for undergoing the proposed boundary detection.

To evaluate the proposed method, the boundaries obtained from the proposed method are compared to the ground truth data degree-by-degree by calculating the correlation of x,y and the radius which measures from the center of an image. The results show that the detected boundaries from the proposed method are correlated with the actual boundary by 93.92%. The overlap of detected boundaries from two methods are shown in Fig. 3. The yellow solid line illustrates the boundary obtained from our proposed method whereas the red dashed line represents the ground truth boundary.

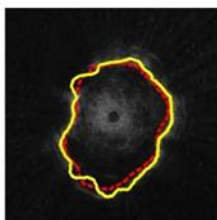


Fig. 3: Overlapping of the boundaries obtained from the proposed method (yellow solid line) and the ground truth data (red dashed line)

Additionally, the study shows that there is not much difference in correlation between benign and malignant lesion data. According to Table 1, the correlation of benign lesion is 93.88% while malignant is 93.96% which yield the total correlation of 93.92%.

Table 1: Correlation of boundary of the proposed method and ground truth data categorized by lesion types

Benign	Malignant	Total
0.9388	0.9396	0.9392

4. Discussion and Conclusions

In summary, this paper proposes a new method to detect the boundary of a lesion which includes polar system transformation, maximum intensity localization, DBSCAN clustering, second order derivatives, smoothing and spline interpolation, to briefly delineate lesion boundary from sample EBUS images. As a result, automatic pulmonary lesion boundary detection from EBUS images is performed successfully and hence can assist radiologists in further process. However, there are some special cases of EBUS images which cause the

detection some problems, and hence, result in lower correlation with ground truth data, such as images with highly presence of air linear bronchogram, as illustrated in Fig. 4(a), and mostly absence of lesion margin as depicted in Fig. 4(b). For the highly presence of air bronchogram, the texture inside lesion is non-uniform and hyperechoic which is difficult to distinguish between boundary and air bronchogram, whereas, in mostly absence of lesion margin, more than 50% of lesion boundary disappear, due to an inappropriate frame selection. Thus, further study may be required to solve these problems. In addition, the study of EBUS images and their defined boundaries will be continued in order to distinguish benign from malignant lesions by considering their ultrasonographic features. Finally, a computer-aided diagnosis (CAD) of lung cancer can be constructed.

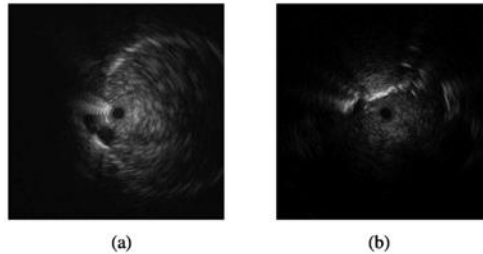


Fig 4: EBUS Image with
 (a) highly presence of air linear bronchogram
 (b) mostly absence of lesion margin

Acknowledgements

This project is financially supported by Centre of Excellence in Mathematics (CEM), Thailand, and the authors are grateful to Phramong Kutklao Hospital, Bangkok, Thailand, for providing all endobronchial ultrasonographic data.

References

- [1] GLOBOCAN 2012 v1.0, Cancer Incidence and Mortality Worldwide: IARC Cancer Base No. 11, Ferlay, J., Soerjomataram, I., Ervik, M., Dikshit, R., Eser, S., Mathers, C., Rebelo, M., Parkin, D. M., Forman, D., Bray, F., International Agency for Research on Cancer; 2013, France, <http://globocan.iarc.fr>
- [2] Aberle, D. R., Adams, A. M., Berg, C. D., Black, W. C., Clapp, J. D., Fagerstrom, R. M. et al., Reduced lung-cancer mortality with low-dose

- computed tomographic screening. *New England Journal of Medicine*, **365**, pp. 395-409, Aug 4 2011.
- [3] What If I Have a Spot on My Lung? Do I Have Cancer? Patient Education Guide, American College of Chest Physicians, 2004, Online. <http://onebreath.org/document.doc?id=36>
- [4] Herth, F. J., Ernst, A., & Becker, H. D., Endobronchial ultrasound-guided transbronchial lung biopsy in solitary pulmonary nodules and peripheral lesions. *European Respiratory Journal*, **20**, pp. 972-4, Oct 2002.
- [5] Yang, M. C., Liu, W. T., Wang, C. H., Lin, H. C., Chen, H. C., Chou, C. L. et al., Diagnostic value of endobronchial ultrasound-guided transbronchial lung biopsy in peripheral lung cancers. *Journal of the Formosan Medical Association*, **103**, pp. 124-9, Feb 2004.
- [6] Lin, S. M., Chung, F. T., Huang, C. D., Liu, W. T., Kuo, C. H., Wang, C. H. et al., Diagnostic value of endobronchial ultrasonography for pulmonary tuberculosis. *Journal of Thoracic and Cardiovascular Surgery*, **138**, pp. 179-84, Jul 2009.
- [7] Shirakawa, T., Imamura, F., Hamamoto, J., Honda, I., Fukushima, K., Sugimoto, M. et al., Usefulness of endobronchial ultrasonography for transbronchial lung biopsies of peripheral lung lesions. *Respiration*, **71**, pp. 260-8, May-Jun 2004.
- [8] Kurimoto, N., Murayama, M., Yoshioka, S. & Nishisaka, T., Analysis of the internal structure of peripheral pulmonary lesions using endobronchial ultrasonography. *CHEST Journal*, **122**, pp. 1887-94, Dec 2002.
- [9] Kuo, C. H., Lin, S. M., Chen, H. C., Chou, C. L., Yu, C. T. & Kuo, H. P., Diagnosis of peripheral lung cancer with three echoic features via endobronchial ultrasound. *CHEST Journal*, **132**, pp. 922-9, Sep 2007.
- [10] Shinagawa, N. et al., Transbronchial biopsy for peripheral pulmonary lesions under real-time endobronchial ultrasonographic guidance. *Journal of Bronchology & Interventional Pulmonology*, **16**(4), pp. 261-265, Oct 2009.
- [11] Ester, M., Kriegel, H. P., Sander, J. & Xu, X., A density-based algorithm for discovering clusters in large spatial databases with noise. Proc. of the Second International Conference on Knowledge Discovery and Data Mining (KDD-96). In Evangelos Simoudis, Jiawei Han, Usama M. Fayyad, AAAI Press, pp. 226-231, 1996.
- [12] Smith, S.W., *Digital Signal Processing: A Practical Guide for Engineers and Scientists* (Chapter 15). Moving Average Filters, Newnes, pp. 277-284, 2003.

VITA

Wannapon Suraworachet is a master's degree student majoring in computer science and information technology at department of mathematics and computer science, faculty of science, Chulalongkorn university. She also graduated in bachelor's degree with the same major in 2011. She is highly motivated and interest in image processing, especially medical imaging, since she believes in innovating technologies that could contribute to the world. Her current field of study is involved lung cancer classification based on endobronchial ultrasound image. Her future works are about discovering significant image features to apply in the computer-aided diagnosis system and extending the system to be adaptable for other kinds of cancer.

